JCTC Journal of Chemical Theory and Computation

ARTICLE

pubs.acs.org/JCTC

Bipolar Reaction Path Hamiltonian Approach for Reactive Scattering Problems

Jeremy B. Maddox*,† and Bill Poirier‡

†Department of Chemistry, Western Kentucky University, Bowling Green, Kentucky, 42101-1079, United States

‡Department of Chemistry and Biochemistry, Texas Tech University, Lubbock, Texas, 79409-1061, United States

ABSTRACT: In this work we present a method for calculating the stationary state wave functions and reaction probabilities of a multidimensional reactive scattering system. Our approach builds upon the counter-propagating wave methodology (CPWM) developed by Poirier and co-workers for calculating one-dimensional stationary state wave functions. The method involves the formulation of a bipolar decomposition for multidimensional stationary scattering wave functions within the context of a reaction path Hamiltonian, so we refer to this work as the bipolar reaction path Hamiltonian (BRPH) approach. Benchmark calculations are presented for several 2D model scattering systems with linear reaction coordinates. We show that the BRPH approach is competitive with conventional calculations based on discrete variable representation (DVR) methods.

1. INTRODUCTION

In this work we formulate a computational approach for calculating the stationary state wave functions and state-to-state reaction probabilities of a multidimensional (multi-D) reactive scattering system.[1] For such problems, the total energy is a continuous quantity and the system exhibits some unbound motion along at least one spatial coordinate. By definition, the stationary state wave functions of the system must simultaneously satisfy both the time-dependent Schrödinger equation (TDSE)

$$i\hbar \frac{\partial \Phi_E}{\partial t} = \hat{H}\Phi \tag{1}$$

and the time-independent Schrödinger equation (TISE)

$$\hat{H}\Phi_E = E\Phi_E \tag{2}$$

where $\hat{H}$ is the Hamiltonian operator corresponding to the total energy of the system and Φ_E is a wave function representing the stationary scattering state with energy E. The spatial and temporal components of Φ_E are formally factorizable. For example, in one-dimensional (1D) space we have

$$\Phi_E(x,t) = \phi_E(x)\mathrm{e}^{-iEt/\hbar} \tag{3}$$

where $\phi_E(x)$ is an amplitude that depends only on the system's spatial coordinate x and also satisfies the TISE.[2] For unbound motion, it is well-known that stationary state wave functions are not square-integrable, and therefore, may not represent a physically realizable state.[3] Nevertheless, stationary scattering states are conceptually important as a formal tool for constructing normalizable wave packets, and they are a useful idealization for the limiting case of a wave packet that has a very narrow profile in momentum space and a spatial width that is much larger than the dimensions of the scattering problem.

In the context of chemical reactions, the "scattering coordinate" (or "reaction coordinate") represents a set of pathways through the molecular configuration space that yield a transformation from reactants to products. The "reaction path" then refers to one such pathway, generally the minimum energy pathway, which connects asymptotic minima in the reactant and product potential valleys via a saddle point corresponding to the transition state. Due to coupling with the other "perpendicular" coordinates or degrees of freedom, motion along the reaction coordinate leads to the rearrangement of chemical bonds and to the many ways in which the internal energy of the system can be redistributed among rotational, vibrational, and electronic degrees of freedom of the reactants and products, thus complicating the details of the scattering process. This is especially true for problems with many atoms and low-lying excited electronic states. At the same time, however, when all is said and done, and the quantum reactive scattering event is completed, there remains the fundamental concept that the molecular collision can be represented by a superposition of incident, transmitted, and reflected waves along the reaction coordinate. Moreover, the amplitude of the transmitted wave is directly related to the reaction probability for a particular scattering channel, which is defined by the asymptotic perpendicular quantum states of the reactants and products. In turn, the amplitudes associated with all energetically accessible channels are related to the reaction cross-section and, ultimately, the overall reaction rate.[4,5]

To compute the various reactive scattering quantities above in accurate quantum dynamical detail, the use of discrete variable representations (DVRs)[6−9] with absorbing boundary conditions (ABCs),[10,11] i.e., complex absorbing potentials, has over the years proven to be a very effective, general approach.[12,13] Variations of the DVR-ABC method have been applied to reactive scattering,[14−17] electron scattering,[18] isomerization reactions,[19] photoreactions,[20−24] nonadiabatic systems,[25] and molecule-surface scattering.[26] Though robust and accurate, the DVR-ABC methods suffer from the well-known limitation of exponential scaling of computational effort with system size, thus limiting such calculations in practice to small molecules. Another major

Received: August 12, 2011
Published: September 21, 2011

difficulty is associated with ABCs, in particular, which necessarily expand the required reaction coordinate ranges substantially, especially in the vicinity of the channel threshold energies. By now, ABCs have been well-developed for the purpose of truncating the computational domain of a given problem as much as possible;[27−29] however, it can still be a nontrivial task to minimize artificial reflections, especially at energies just above threshold.

In this paper, we develop an exact computational method for determining the stationary states and reaction probabilities for a certain class of multi-D reactive scattering problems with linear and quasilinear reaction coordinates (future work will address the curvilinear case). As we shall see, this method naturally incorporates the boundary conditions of the physical scattering problem, so that there is no need for ABCs and the attendant expansion of reaction coordinate space. The method is also designed to scale well with increasing system size, provided some approximations (albeit fairly minor and reasonable) are introduced. Our approach builds upon the bipolar counter-propagating wave methodology (CPWM) of Poirier and co-workers, which for scattering problems involves the decomposition of stationary states into so-called "bipolar" traveling wave components. Over the last several years, various CPWM schemes have been developed and applied to bound stationary states,[30] scattering states in 1D,[31−33] nonadiabatic dynamics,[34] multi-D scattering,[35] and nonstationary state dynamics.[36−38] Although these represent a great improvement over traditional unipolar quantum trajectory methods[39] and have enabled the first-ever accurate synthetic quantum trajectory calculations to be performed for a system with substantial reflection interference,[37,38] they still can exhibit certain practical difficulties when applied to real molecular systems, such as occasional numerical instabilities or inaccuracies, thus motivating the development of new bipolar approaches.

The present work involves the formulation of a bipolar CPWM for multi-D systems in terms of adiabatic vibrational eigenstates associated with bound motion in the perpendicular degrees of freedom and a corresponding Hamiltonian that varies parametrically along a suitably defined reaction path. Some time ago, Miller and co-workers developed an approximate representation for the molecular Hamiltonian along the reaction path of a reactive system that could be constructed using a reasonable number of accurate electronic structure calculations.[40] By now, the reaction path Hamiltonian (RPH) approach is essentially a cornerstone of both classical and quantum mechanical theories of kinetic rates constants, and extensions of the basic RPH notion continue to be actively developed.[41−44] The RPH is sufficiently general that it can be applied within the context of many different computational schemes, such as self-consistent field calculations[45,46] and, in a more recent example, diffusion Monte Carlo.[47] In our work, we apply the bipolar CPWM approach to scattering problems within a framework that will be suitable for the RPH approximation; hence, we refer to this method as the bipolar reaction path Hamiltonian (BRPH) approach.

The organization of the rest of this paper is as follows. In section 2 we highlight some key points of bipolar CPWMs for 1D scattering problems. This background information is important for understanding the theoretical and numerical developments associated with the BRPH approach that are described in section 3. Some additional theoretical details are provided in Appendices A and B. We present and discuss several benchmark numerical calculations in section 4, where the state-to-state reaction probabilities are determined for model problems involving scattering motion across Eckart-type barriers with coupling to harmonic vibrational motion. The BRPH results for these problems are quantitatively compared with analytical theory and corresponding DVR-ABC calculations. Appendix C describes our implementation of the DVR-ABC method. Finally, in section 5 we conclude with a brief summary and outlook for future studies involving more realistic problems with curvilinear reaction coordinates and larger dimensionalities.

2. THE 1D COUNTER-PROPAGATING WAVE METHODOLOGY (CPWM)

A thorough discussion of the CPWM for scattering problems can be found in the literature,[31−33,35] and we will not repeat all of those details here. However, we must summarize a few key concepts that are necessary to understand the new developments presented in section 3 for multi-D scattering problems. In 1D scattering problems, the Hamiltonian is given by

$$\hat{H} = -\frac{\hbar^2}{2m}\frac{\mathrm{d}^2}{\mathrm{d}x^2} + V(x) \tag{4}$$

where x represents the scattering coordinate for a particle with mass m that traverses the barrier potential V. Furthermore, we take V to be an asymptotically convergent function, i.e., $V(x \rightarrow \pm\infty) =$ constant(s).[48]

In the CPWM approach, the stationary scattering states of the system are represented by an appropriate superposition of counter-propagating traveling waves, such as

$$\Phi(x,t) = \Phi_+(x,t) + \Phi_-(x,t) \tag{5}$$

We refer to this as a bipolar decomposition, and $\Phi_\pm$ are the bipolar components. Note that we have now omitted the explicit reference to E in our notation for Φ and $\Phi_\pm$; henceforth, this energy dependence is implied. If we assume a left-incident scattering convention, then the Φ_+ component represents a traveling wave that moves with positive momentum (to the right) and asymptotically corresponds to the incident and transmitted plane wave portions of the total wave function. Conversely, the Φ_- component moves with negative momentum (to the left) and is associated with a reflected plane wave in the left asymptote and approaches zero in the right asymptote. The interference between the two bipolar components determines the form of the total stationary state wave function.

For the 1D scattering problems described above, the bipolar components may be expressed as

$$\Phi_\pm(x,t) = \alpha_\pm(x)\exp\left(\pm\frac{\mathrm{i}}{\hbar}\int p(x)\,\mathrm{d}x - \frac{\mathrm{i}}{\hbar}Et\right) \tag{6}$$

where $\alpha_\pm$ are a pair of amplitudes that vary over the same region of space as the scattering potential. Asymptotically, these amplitudes should become constant and will be related to the overall transmission and reflection probabilities at a given energy. In eq 6, notice that the $\alpha_\pm$ amplitudes have been formally separated from the oscillatory parts of the wave function, which are represented by the complex exponential factors. The integral term in the exponent represents the classical action of a particle with momentum $p = (2m(E - V_{\mathrm{eff}}))^{1/2}$ moving in an effective potential field $V_{\mathrm{eff}}(x)$. Different bipolar decompositions may be specified by choosing different forms for V_{eff}, provided that $E > V_{\mathrm{eff}}(x)$ for all x and that $V_{\mathrm{eff}}(x \rightarrow \pm\infty) = V(x \rightarrow \pm\infty)$. Aside from these constraints, which guarantee that $\Phi_\pm$ have the correct asymptotic

behavior, the effective potential is more or less arbitrary.[49] Note that the requirements on $V_{\mathrm{eff}}(x)$ do not imply that the true potential, $V(x)$, must be less than the energy; i.e., tunneling, even deep tunneling, is in principle allowed and treated exactly.

Even for a given V_{eff}, the bipolar decomposition described above does not provide a unique specification of the $\Phi_{\pm}$, although the allowed form of these is greatly constrained. To obtain a unique decomposition, leading to slowly varying $\alpha_{\pm}(x)$, we must impose an additional relation

$$\Phi' = -\frac{p'}{2p}\Phi + \frac{\mathrm{i}}{\hbar}p(\Phi_+ - \Phi_-) \tag{7}$$

which was originally introduced by Fröman and Fröman (FF) in the context of a generalized semiclassical theory for tunneling phenomena.[50] In eq 7 and hereafter we use a prime to denote the derivative of a 1D function with respect to the scattering coordinate, e.g., $f' = \mathrm{d}f(x)/\mathrm{d}x$.

Starting from an essentially arbitrary initial guess for $\Phi_{\pm}$, the exact FF decomposition solution $\Phi_{\pm}$ are obtained in the long-time limit by solving a pair of time-dependent equations of motion (see eq 10 below), involving the total (hydrodynamic) time derivatives of the bipolar components

$$\mathrm{d}_t\Phi_{\pm} = \partial_t\Phi_{\pm} \pm \frac{p}{m}\Phi'_{\pm} \tag{8}$$

The notation d_t signifies the total time derivative and implies that $\Phi_{\pm}$ are evolving on a pair of counter-propagating Lagrangian-type reference frames $x_{\pm}(t)$ that satisfy the following auxiliary equations of motion, defining the left- and right-traveling trajectories

$$\mathrm{d}_t x_{\pm} = \pm\frac{p}{m} \tag{9}$$

Using the FF condition and the TISE to expand the convective term $\Phi'_{\pm}$ leads to the following coupled equations of motion

$$\mathrm{d}_t\Phi_{\pm} = F_{\pm}\Phi_{\pm} + G(\Phi_+ + \Phi_-) \tag{10}$$

where the factors $F_{\pm}$ and G depend on V_{eff} according to

$$F_{\pm} = \frac{\mathrm{i}}{\hbar}\left(E - 2V_{\mathrm{eff}} \mp \frac{\mathrm{i}\hbar V'_{\mathrm{eff}}}{\sqrt{8m(E - V_{\mathrm{eff}})}}\right) \tag{11a}$$

$$G = -\frac{\mathrm{i}}{\hbar}\left(V - V_{\mathrm{eff}} - \frac{\hbar^2}{8m}\left[\frac{V''_{\mathrm{eff}}}{E - V_{\mathrm{eff}}} + \frac{5}{4}\left(\frac{V'_{\mathrm{eff}}}{E - V_{\mathrm{eff}}}\right)^2\right]\right) \tag{11b}$$

The solutions of eq 10 are subject to the boundary conditions

$$\Phi_+(x \to -\infty, t) = \exp\left[\frac{\mathrm{i}}{\hbar}\int p\,\mathrm{d}x - \frac{\mathrm{i}}{\hbar}Et\right] \tag{12a}$$

$$\Phi_-(x \to +\infty, t) = 0 \tag{12b}$$

that serve to reinforce the left-incident scattering convention. Given an initial guess for $\Phi_{\pm}(x,t{=}0)$, the dynamics that follows from eq 10 can be viewed as a pseudo-time-dependent relaxation brought about through the cooperative influence of G, which couples the evolution of $\Phi_{\pm}$, and the application of the boundary conditions.

To help illustrate this, we suppose that the "initial" ($t = 0$) bipolar components are represented by a Φ_+ plane-wave with constant positive momentum $p_0 = (2m(E - V(-\infty)))^{1/2}$, and a Φ_- reflected wave with zero amplitude:

$$\Phi_+(x, t = 0) = \exp\left(\frac{\mathrm{i}}{\hbar}p_0 x\right) \tag{13a}$$

$$\Phi_-(x, t = 0) = 0 \tag{13b}$$

Clearly, the superposition of these components is not a stationary state solution of the TISE for $V(x) \neq 0$. Asymptotically, G is negligible, and the coupling between the bipolar components vanishes; therefore, $\Phi_{\pm}$ evolve like free-particle wave functions in those regions. This evolution is enforced by the boundary conditions and the motion of the counter-propagating reference frames, which carry the $\Phi_{\pm}$ amplitude away from the interaction region in opposite directions. Within the interaction region, however, where $G \neq 0$, there is coupling that leads to a transfer of amplitude between the $\Phi_{\pm}$ components, and over time a nonzero reflected wave builds up. Eventually a steady-state is reached between the flux associated with the boundary conditions and the flux induced by the coupling. The long-time limit solutions of the CPWM equations of motion provide a pair of bipolar components whose superposition is the desired stationary scattering state wave function.

Figures 1 and 2 illustrate typical CPWM results for the case of a particle with mass $m = 2000$ au scattering across a 1D Eckart barrier defined by

$$V(x) = V_0\,\mathrm{sech}^2(\alpha x) \tag{14}$$

where $V_0 = 0.0018$ hartree and $\alpha = 3.0\ \mathrm{b}^{-1}$. This parametrization of the Eckart potential has been referred to as the Eckart A barrier in previous work.[32,33] The potential is plotted in Figure 1a as a function of x in units of V_0, and the area beneath the curve has been shaded.

We have numerically integrated the so-called "constant velocity" form of the CPWM equations,[31−33] where $V_{\mathrm{eff}}(x) = 0$ for all x, starting from the initial conditions given in eq 13. The bipolar solutions are represented on a grid of equally spaced points with grid spacing Δx, and the time step is defined by $\Delta t = \Delta x(m/2E)^{1/2}$. The solutions are propagated in time using a second-order Runge−Kutta method until the probability densities of the bipolar components $\rho_{\pm} = |\Phi_{\pm}|^2$ are essentially fully converged. For this work, we have calculated the bipolar components using $\Delta x = 0.02$, 0.01, 0.005, and 0.0025 b for 20 stationary states with energies in the range of 10−200% of the barrier height.

The $\rho_{\pm}$ densities for the stationary state with energy $E = V_0$ (and $\Delta x = 0.0025$ b) are plotted as the solid and dashed lines in Figure 1a along with the total probability density $\rho = |\Phi|^2 = |\Phi_+ + \Phi_-|^2$, which is represented by the dotted line. Clearly, the $\rho_{\pm}$ densities are constant in the asymptotic regions and vary more or less smoothly across the range of the potential barrier. The total density ρ oscillates in the region to the left of the barrier because of interference between the $\Phi_{\pm}$ components. On the right-side of the barrier the reflected wave vanishes and there is no interference. Here, the value $\rho_+(x\to\infty)$ is related to the transmission probability P_{T}, and the value $\rho_-(x\to-\infty)$ is related to the reflection probability P_{R}. In practice, these quantities are estimated at the edges of the numerical grid ($x = \pm 3.085$ b in this case). In principle, the 1D CPWM above is exact, so these quantities as well as $\Phi_{\pm}$ may be computed to arbitrary precision, via a suitable choice of the numerical parameters (grid edges, grid spacing, time step, etc.).

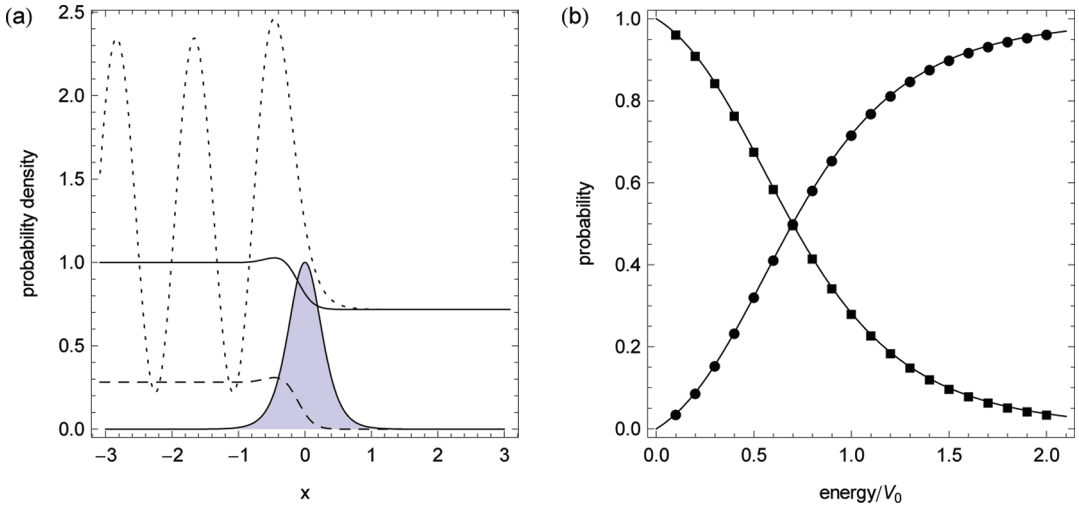

Figure 1. (a) The (solid) ρ_+, (dashed) ρ_-, and (dotted) ρ probability densities corresponding to the $E = V_0$ stationary scattering state of the 1D Eckart barrier are plotted as a function of position x in units of bohr. The barrier height is $V_0 = 0.0018$ hartree, and the shaded area shows the potential function in units of V_0. (b) Benchmark CPWM results for the transmission (P_T, circles) and reflectance (P_R, squares) probabilities as a function of energy for 20 stationary states of the 1D Eckart barrier. The grid spacing for these results is $\Delta x = 0.0025$ b. The solid curves corresponds to the exact result for this problem.

In Figure 1b we plot the calculated P_T and P_R (circles and squares, respectively) as a function of energy in units of the barrier height, and the solid lines correspond with analytical results.[51] As expected, P_T increases (P_R decreases) with increasing energy, and qualitatively, there is good agreement between the present CPWM results and exact theory. In Figure 2a we show the fractional error in P_T as a function of energy for several values of the CPWM grid spacing. This error is computed according to the formula

$$(P_T)_{error} = \frac{1}{P_T}|P_T^{calc} - P_T| \tag{15}$$

where P_T^{calc} is the calculated transmission probability and P_T is the corresponding exact result. The error is generally larger at lower energies, where the time steps are are also larger, and the sporadically low errors, e.g., at $E = 0.5V_0$, are likely due to a fortuitous cancellation that can occur when the error changes sign. The fractional errors in P_T are less than 0.1% across the given energy range for all grid spacings, and at a given energy, the error is reduced by about half an order of magnitude as Δx is decreased by a factor of one-half.

One advantage of working with stationary scattering states is that the asymptotic form of the wave functions and the energy of the system are known in advance. This fact can be used in different ways to estimate the numerical error in calculations for which analytical results are unavailable. Panels b−d of Figure 2 illustrate three additional fractional error measures as a function of energy for different grid spacings. If the exact values of P_T are not known, then the error can be estimated by calculating P_T and P_R from $\rho_+(x_{max})$ and $\rho_-(x_{min})$, respectively, and comparing with the exact relationship $P_T + P_R = 1$. The normalization errors for the present calculations are shown in Figure 2b, where it is seen that this error estimate increases very regularly with increasing energy. Also, the normalization error for this problem drops by a full order of magnitude as the grid spacing decreases by a factor of one-half.

For the second error estimate, we note that the bipolar superposition should constitute a solution of the TISE, and we can use an independent numerical method to compute the expectation value of the energy from the CPWM stationary state. The points shown in Figure 2c represent the error associated with the energy expectation value for different grid spacings. These errors are computed according to the formula

$$\langle \hat{H} \rangle_{error} = \frac{1}{E}\left| E - \frac{\int \Phi^*(x)\hat{H}\Phi(x)\,dx}{\int \Phi^*(x)\,\Phi(x)\,dx} \right| \tag{16}$$

where the operation of the Hamiltonian is evaluated using fourth-order finite difference derivatives for the kinetic energy term and Boole's method for the numerical integrations.[52] In this way, the error estimate is averaged over the entire stationary state via numerical integration. These calculations do introduce additional errors; however, because the grid spacings are relatively small, such errors are expected to be less significant than the error in the CPWM calculations. For the given energy range, we see that the fractional error is less than 0.1% and decreases with the grid spacing in the same fashion as the fractional error in P_T. For the third error estimate, we note that the FF condition must also be satisfied at long times. Equation 7 can be rearranged and combined with $p = (2mE)^{1/2}$ to solve for the system's energy, and this provides another independent method to estimate the error. The points shown in Figure 2d represent the error associated with how well the FF condition is satisfied according to the equation

$$FF_{error} = \frac{1}{E}\left| E + \frac{\hbar^2}{2m}\left| \frac{\int \Phi(x)\,\Phi'(x)\,dx}{\int \Phi^*(x)(\Phi_+(x) - \Phi_-(x))\,dx} \right|^2 \right| \tag{17}$$

where we have used finite differences and numerical integration to perform the error calculation. These fractional errors follow the same trend as the error in the energy expectation value; however, these results show that the calculated bipolar CPWM solutions are internally consistent with the FF condition.

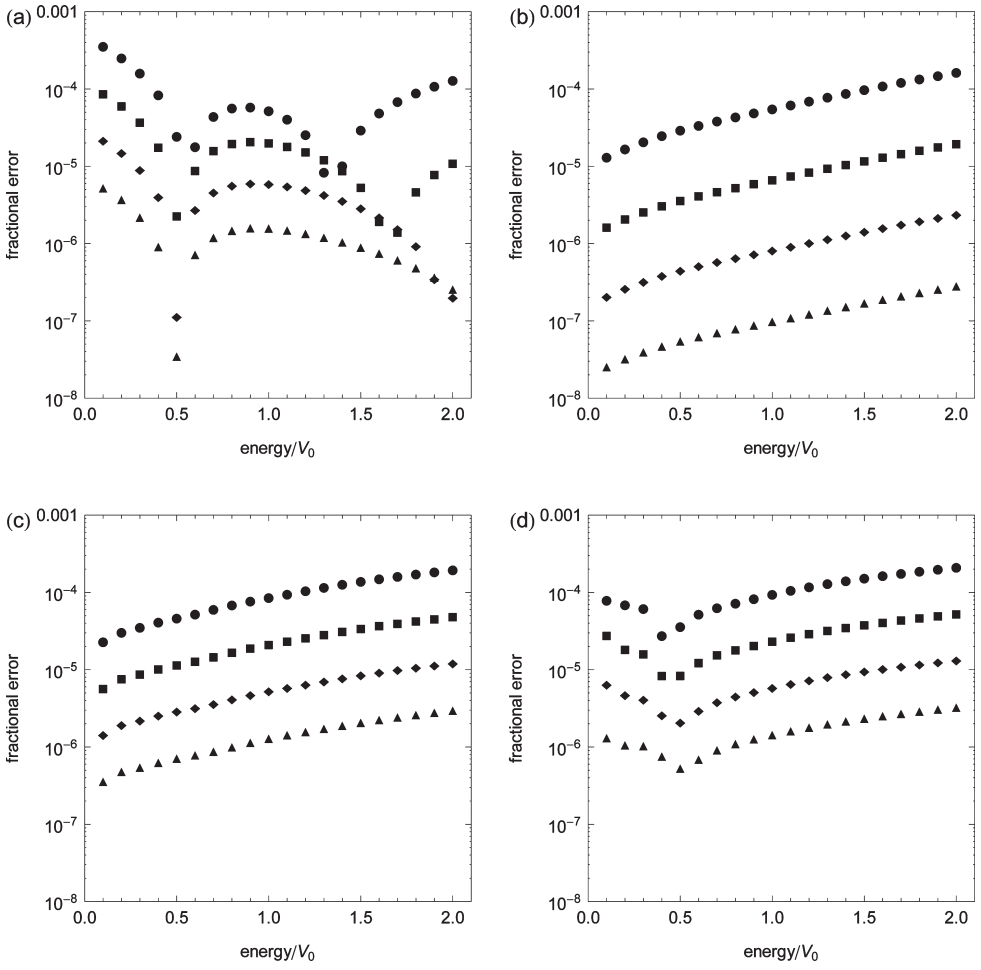

Figure 2. Various fractional error measures for the 1D Eckart A problem as a function of energy and for several different CPWM grid spacings Δx: (circles) 0.02, (squares) 0.01, (diamonds) 0.005, and (up-triangles) 0.0025 in units of bohr. (a) Fractional error measure in the calculated transmission probability P_T. (b) Fractional error associated with the normalization condition $P_T + P_R = 1$. (c) Fractional error estimate associated with the expectation value of the Hamiltonian. (d) Fractional error estimate associated with the FF condition.

Finally, we note that all of these errors can be reduced by employing a wider grid, smaller grid-point spacings, or smaller time steps in order to achieve higher accuracy, and it is not necessary to adjust these in a nonlinear way to improve the convergence. This is not the case for ABCs, where there are subtleties associated with finessing the onset of the absorbing potential, its width, height, and general shape. Also, of course, the coordinate range needed here for a given level of accuracy is always much smaller than if an ABC were used.

3. THE BIPOLAR REACTION PATH HAMILTONIAN (BRPH) APPROACH

In this section we formulate the BRPH approach for the simplest class of multi-D reactive scattering problems; namely, a 2D system with a linear reaction coordinate. We also present a discussion of our numerical implementation for the calculation of stationary state wave functions involving multiple scattering channels and state-to-state reaction probabilities, i.e., the probabilities associated with elements of the scattering matrix (S-matrix). Our general strategy is to transform the 2D scattering problem into a corresponding 1D multichannel scattering problem, involving individual channel scattering amplitudes defined along a suitably chosen linear reaction path. We invoke a bipolar representation for each channel scattering amplitude, and this leads to a set of coupled equations of motion that are formally similar to the 1D CPWM equations described in section 2. Hence, we can then exploit the same numerical algorithms for 1D scattering problems to determine the stationary state wave functions of the 2D problem.

3.1. Theory. We consider a two-dimensional (2D) scattering problem described in some appropriately chosen mass-weighted Cartesian (MWC) coordinate system. In this case, the Hamiltonian operator has the form

$$\hat{H} = -\frac{\hbar^2}{2m}\left(\frac{\partial^2}{\partial x^2} + \frac{\partial^2}{\partial y^2}\right) + V(x,y) \tag{18}$$

where m is the reduced mass and V is a 2D potential energy surface. For realistic problems, such as the collinear A + B−C → A−B + C exchange reaction, the potential will necessarily exhibit a bend in the MWC space.[5] However, in the present work, we limit our consideration to the simplified case, where the reaction

path is both linear and parallel to the x-axis. The x (reaction) coordinate is then directly associated with some unbound scattering motion across a potential barrier, and the y (perpendicular) coordinate is associated with bound vibrational motion. Also, we must require that V approach a function that is independent of x in each asymptotic limit, and we further assume (for this paper) that this scattering potential is asymptotically symmetric, i.e., $V(x\rightarrow\pm\infty,y) = V_{\text{asymp}}(y)$. As discussed in section 2 and below, the latter assumption allows us to utilize the constant velocity CPWM approach (where $V_{\text{eff}} = 0$), which leads to a more natural approach for the benchmark problems described in section 4. Extension of the following formulation to the more general case of an asymptotically asymmetric problem is relatively straightforward but involves details that have already been addressed in previous work.[33]

Next, we introduce a set of vibrational states that vary slowly, i.e., adiabatically, along the reaction coordinate. Note that this does not imply that we are assuming that the vibrational quantum number of the stationary state be conserved as a function of x. The adiabatic vibrational states are the solutions of a corresponding adiabatic TISE

$$\left[-\frac{\hbar^2}{2m}\frac{\partial^2}{\partial y^2} + V(x,y)\right]\phi_i(x,y) = \varepsilon_i(x)\,\phi_i(x,y) \tag{19}$$

where both the eigenvalues ε_i and the wave functions ϕ_i depend parametrically on x.[53] Our assumptions on the 2D potential imply that $\varepsilon_i(x) \rightarrow E_i$ as $x \rightarrow \pm\infty$, where E_i are the eigenenergies of the asymptotic system with potential energy V_{asymp}. It is further assumed that these adiabatic eigenstates can be determined exactly or by some appropriate approximation, and it is this last point where we can make a connection to the RPH method. For example, if only the potential energy, force, and Hessian were known along the reaction path, then the adiabatic eigenstates could be approximately represented with harmonic oscillator wave functions.

The key ansatz within the BRPH approach is that the total stationary scattering state for a given energy E can be written as an infinite sum over the adiabatic eigenfunctions

$$\Phi(x,y,t) = \sum_i^{\infty} a_i(x,t)\,\phi_i(x,y) \tag{20}$$

and we refer to the set of 1D functions a_i as channel scattering amplitudes. Each channel scattering amplitude is then expressed as a superposition of bipolar components:

$$a_i(x,t) = a_{i+}(x,t) + a_{i-}(x,t) \tag{21}$$

where $a_{i\pm}$ take the form of traveling waves that move in opposite directions along the reaction coordinate x. If the potential energy meets the criteria discussed above, then it is sensible to set $V_{\text{eff}} = 0$ and invoke the constant velocity form for the bipolar components

$$a_{i\pm}(x,t) = \alpha_{i\pm}(x)\exp\left[\frac{\mathrm{i}}{\hbar}(\pm p_i x - Et)\right] \tag{22}$$

where $p_i = (2m(E - E_i))^{1/2}$ is the momentum of a particle with mass m and kinetic energy $E - E_i$. Similar to the 1D case, the oscillatory components of eq 22 are formally separated from the $\alpha_{i\pm}$ amplitudes, and these are expected to vary over the interaction region and asymptotically converge to values that may then be related to the elements of the **S**-matrix.

There are several points here that merit further discussion. First, we have presumed that the adiabatic energy eigenvalues form a discrete spectrum; however, the adiabatic Hamiltonian may also possess states corresponding to a continuous range of eigenenergies if the perpendicular degrees of freedom are semibound. Such considerations will be saved for our future work, and here we will only consider the discrete case. Second, in practice, we cannot numerically represent an infinite number of adiabatic states, so we will have to truncate the sum in eq 20 at some point in order to carry out feasible calculations. We expect the number of terms included will affect both the computational effort and the convergence associated with numerical results and that this may lead to various approximation strategies for different types of scattering problems. Finally, for a given total energy E, both open channel $E_i < E$ and closed channel $E_i > E$ scattering amplitudes contribute to the sum in eq 20. For open channels, the momenta p_i are real-valued and the bipolar components $a_{i\pm}$ contain complex exponentials that oscillate with respect to position. For closed channels the p_i are imaginary and $a_{i\pm}$ contain real-valued exponentials. Both cases must be included if the total stationary state is to be represented exactly, and it is clear that the spatial amplitudes $\alpha_{i\pm}$ must vanish asymptotically for closed channels. Next, we develop the equations of motion for the bipolar components of the channel scattering amplitudes.

First, the FF condition is applied as a separate condition for each channel scattering amplitude

$$a_i' = \frac{\mathrm{i}}{\hbar}p_i(a_{i+} - a_{i-}) \tag{23}$$

which along with the TISE, provide the necessary relationships to develop a set of coupled time-dependent equations of motion for the bipolar components. To accomplish this, we appeal to an adiabatic representation of the 2D Hamiltonian. The details of the derivation are provided in Appendix A and the resulting equations of motion are given by

$$\mathrm{d}_t a_{i\pm} = F_i a_{i\pm} + G_i a_i + H_i \tag{24}$$

Before discussing the individual terms here, we consider the general structure of these equations, and in particular, the total time derivative:

$$\mathrm{d}_t a_{i\pm} = \partial_t a_{i\pm} \pm \frac{p_i}{m}a_{i\pm}' \tag{25}$$

Like the 1D CPWM equations, this expression implies that the bipolar components $a_{i\pm}$ are evolving within a set of corresponding Lagrangian reference frames $x_{i\pm}(t)$ that satisfy the ancillary equations of motion

$$\mathrm{d}_t x_{i\pm} = \pm\frac{p_i}{m} \tag{26}$$

whose solutions move in opposite directions for the $\pm$ components and with different constant velocities $v_i = p_i/m = (2(E - E_i)/m)^{1/2}$ for different channel scattering amplitudes. For open channels, the Lagrangian dynamics is more or less similar to the 1D case. For the closed channels, however, where $E_i > E$, there is an apparent problem that the velocities are imaginary. The solutions of eq 26 for the closed channel components can be expressed as

$$x_{i\pm}(t) = x_{i\pm}(0) \pm \mathrm{i}|v_i|t \tag{27}$$

which are complex for real values of t. This may be avoided, however, if we impose the requirement that the closed channel components evolve in imaginary time, i.e., if $t = -\mathrm{i}|t|$, then the closed channel trajectories will be real provided that the initial conditions $x_{i\pm}(0)$ are also real. This and other important issues will be discussed further in section 3.2, where our numerical strategy is described in detail. A similar strategy was employed, and justified, in a previous study.[31] For now, we will continue with an analysis of the terms in eq 24.

The various factors in the BRPH equations of motion are given by

$$F_i = \frac{\mathrm{i}}{\hbar}(E - 2E_i) \tag{28a}$$

$$G_i = -\frac{\mathrm{i}}{\hbar}(\varepsilon_i - E_i) \tag{28b}$$

$$H_i = \frac{\mathrm{i}\hbar}{2m}\sum_j I_{ij}^{(1)} a_j' + I_{ij}^{(0)} a_j \tag{28c}$$

The F_i terms are associated with free particle motion and provide a flux of amplitude both into and out of the scattering region. The G_i terms also play a role in determining how the bipolar components evolve within the scattering region. Most importantly, they provide a coupling between left- and right-traveling components of a given scattering channel, i, leading to intrachannel reflection. This coupling becomes significant in the region of space where the $\varepsilon_i(x)$ deviates significantly from E_i. Finally, the H_i terms provide nonadiabatic coupling across different scattering channels, leading to the redistribution of vibrational energy along the scattering coordinate. Analogous terms are found within certain implementations of the 1D CPWM for applications to scattering systems involving multiple diabatic electronic states.[34] The nonadiabatic coupling terms presented here involve the functions

$$I_{ij}^{(1)}(x) = 2\int \phi_i^*(x,y)\, \phi_j^{(1,0)}(x,y)\, \mathrm{d}y \tag{29a}$$

$$I_{ij}^{(0)}(x) = \int \phi_i^*(x,y)\, \phi_j^{(2,0)}(x,y)\, \mathrm{d}y \tag{29b}$$

that depend on various overlap integrals between the adiabatic wave functions and their spatial derivatives with respect to the reaction coordinate. Within the integrands, the notation $\phi_j^{(m,n)}(x,y)$ represents a mixed partial derivative with respect to x and y

$$\phi_j^{(m,n)}(x,y) = \left(\frac{\partial^m}{\partial x^m}\left[\left(\frac{\partial^n \phi_j(x,y)}{\partial y^n}\right)_x\right]\right)_y \tag{30}$$

and the integrals are labeled with superscripts according to a correspondent spatial derivative of the channel scattering amplitudes. For example, in eq 28c the $I_{ij}^{(1)}$ factor is paired with a'_j and the $I_{ij}^{(0)}$ factor is paired with a_j. These integrals are significant in regions of space where the adiabatic eigenfunctions (but not necessarily eigenenergies) are changing, i.e., regions where motion along x and y are strongly coupled through the scattering potential, $V(x,y)$.

There are several important and interesting limiting cases to consider. The first of these involves the asymptotic behavior of the BRPH equations and the boundary conditions for the bipolar components. For a given energy E, there will be $i_{\max}$ open scattering channels that satisfy $E > E_i$, and therefore a total of $i_{\max}$ degenerate left-incident solutions, i.e., one per open channel. The numerical solution for each such degenerate state requires a separate BRPH calculation with distinct initial and boundary conditions. For the solution left-incident on channel n, the boundary conditions are given by

$$a_{i+}(x \to -\infty, t) = \delta_{in} \exp\left[\frac{\mathrm{i}}{\hbar}(p_n x - Et)\right] \tag{31a}$$

$$a_{i-}(x \to +\infty, t) = 0 \tag{31b}$$

and a set of working initial conditions may be defined as

$$a_{i+}(x, t = 0) = \delta_{\mathrm{in}} \exp(\mathrm{i}p_n x/\hbar) \tag{32a}$$

$$a_{i-}(x, t = 0) = 0 \tag{32b}$$

As $x \to \pm\infty$, the adiabatic eigenenergies and eigenfunctions, by definition, become constant with respect to x. Hence, the G_i and H_i terms will vanish, and the resulting equations of motion in x, i.e., eq 24, are consistent with free-particle evolution. In the long-time limit, the $a_{i\pm}$ solutions reach a steady state, and the **S**-matrix elements can be calculated from the asymptotic values. The transmission probability from state n to state j (state-to-state reaction probability) is given by

$$P_{n\to j} = \sqrt{\frac{E - E_j}{E - E_n}}\,|a_{j+}(x \to +\infty)|^2 \tag{33}$$

Partially state resolved and cumulative reaction probabilities can be calculated by taking different summations of the state-to-state reaction probabilities.

A second interesting limit involves the reduction of the system from a 2D problem to a 1D problem, such as for the case where the system becomes highly confined along y. Here, the adiabatic eigenenergies will be vastly separated from one another so that the only open scattering channel will be the ground state ($i = 0$) of the asymptotic system. The asymptotic zero-point energy E_0 is an arbitrary quantity and may be set to zero without consequence, and the asymptotic excited state energies become infinite by comparison $E_{i\neq 0} \to \infty$. The closed channel scattering amplitudes have imaginary momenta $p_{i\neq 0} = \mathrm{i}|p_i|$, where $|p_{i\neq 0}| = (2m|E - E_i|)^{1/2} \to \infty$ in the highly confined limit. According to eq 22, $a_{i\neq 0,+} \to 0$ for all x, and the $a_{i\neq 0,-}$ will either be divergent if $\alpha_{i\neq 0,-} \neq 0$ or vanish if $\alpha_{i\neq 0,-} = 0$. The former case is unphysical; therefore, all closed channel scattering amplitudes must vanish as the system is reduced to 1D. In this case, the nonadiabatic term H_0 also reduces to

$$H_0 = \frac{\mathrm{i}\hbar}{2m} I_{00}^{(1)} a_i' + I_{00}^{(0)} a_i \tag{34}$$

By expanding the adiabatic eigenfunctions in eq 29a using any complete and orthonormal set of 1D basis functions along y, it can be shown in general that the function $I_{ii}^{(1)} = 0$, for all i and for all x; however, the function $I_{ii}^{(0)}$ is generally nonzero. The quantity $\varepsilon_0 - I_{00}^{(0)}$ takes the role of a 1D scattering potential, and the BRPH equations reduce to

$$\mathrm{d}_t a_{0\pm} = -\frac{\mathrm{i}}{\hbar} E a_{0\pm} - \frac{\mathrm{i}}{\hbar}(\varepsilon_i - I_{00}^{(0)}) a_0 \tag{35}$$

which are formally equivalent to the 1D constant velocity CPWM equations.

A third interesting limit is that of a separable potential, $V(x,y) = V_x(x) + V_y(y)$, for which the adiabatic eigenfunctions, $\phi_i(x,y)$, are independent of x, but the eigenenergies, $\varepsilon_i(x) = E_i + V_x(x)$, need not be. In this case, the H_i terms obviously vanish completely, so there are no nonadiabatic transitions, as is appropriate.

3.2. Numerical Implementation. Next we present our numerical implementation of the BRPH approach. Before solving the BRPH equations, we must first determine the eigenenergies and eigenfunctions of the adiabatic Hamiltonian as a function of the reaction path. For model problems, such as the harmonic and Morse oscillators, this can be done analytically, and relevant formulas for the harmonic case are given in Appendix B. For more general problems, however, one must resort to approximations or numerical calculations. In our development work we have employed DVRs to calculate eigenstate wave functions of the adiabatic Hamiltonian. Here a set of grid points is defined along the reaction path x and we use Colbert and Miller's "universal DVR" with equally spaced grid points to define the matrix elements of the kinetic energy operator for motion along the y-coordinate

$$T^{(y)}_{\alpha\beta} = \frac{(-1)^{\alpha-\beta}}{2m\Delta y^2}\begin{cases} \dfrac{\pi^2}{3} & \alpha = \beta \\ \dfrac{2}{(\alpha-\beta)^2} & \alpha \neq \beta \end{cases} \tag{36}$$

where Δy is the grid spacing and the indices α and β run over interior DVR grid points.[54] The potential energy is approximated as a diagonal matrix over the DVR grid points $V^{(y)}_{\alpha\beta} = V(x,y_\alpha)\delta_{\alpha\beta}$ and varies parametrically with the reaction coordinate. For each grid point along x the perpendicular DVR Hamiltonian, with elements $H^{(y)}_{\alpha\beta} = T^{(y)}_{\alpha\beta} + V^{(y)}_{\alpha\beta}$, is diagonalized to give a finite set of eigenvalues ε_i and DVR eigenvectors ϕ_i^{DVR}. To obtain the desired eigenfunctions, the eigenvectors are multiplied by the appropriate weights, which in this case are related to the grid spacing

$$\phi_i(x,y_\alpha) = \frac{[\phi_i^{\mathrm{DVR}}]_\alpha}{\sqrt{\Delta y}} \tag{37}$$

Numerically speaking, the sign of the DVR eigenvectors is irrelevant, such that $\pm\phi_i^{\mathrm{DVR}}$ are equivalent, and typical numeric algorithms will give results with arbitrary sign at different points along the reaction coordinate. We must be careful to correct this sign mismatch before postprocessing these quantities. The integrands of eq 29 involve the first and second derivative of the adiabatic wave functions with respect to x. These can be efficiently calculated using the DVR representation of the appropriate derivative operators and the inherent quadrature properties of the DVR approach or by using finite difference derivatives and common numerical integration formulas.

The BRPH solutions are represented over a uniform spatial grid with spacing that covers the range over which the scattering potential is numerically significant. This grid should be large enough that the calculated reaction probabilities are converged, and the grid spacing Δx should be small enough to achieve the desired accuracy. This is also important for calculating the spatial derivatives in the nonadiabatic coupling term H_i. Notably, these derivatives involve the total channel scattering amplitudes $a'_i = a'_{i+} + a'_{i-}$, which can be evaluated using either finite differences or the FF conditions. We have implemented both strategies and found that using the FF conditions leads to a more stable convergence of the BRPH solutions compared to finite differences, especially for energy values close to the onset of a channel threshold. For the results discussed in section 4 we have used the FF conditions to evaluate the derivative terms in H_i.

As we have noted, the BRPH equations of motion are expressed in a Lagrangian reference frame, and this means that the $\Phi_{i\pm}$ components are moving in opposite directions and with different velocities $v_i = (2(E - E_i)/m)^{1/2}$ for different channels. The grid points over which these functions are represented move with the flow of the BRPH components so that at different times the grid points for different $a_{i\pm}$ will no longer be coincident with one another. Moreover, for closed channel amplitudes, the velocity is imaginary and we must invoke imaginary time propagation to keep the associated reference frames on the real axis. For an arbitrary universal time step Δt (and $-i|\Delta t|$), we would need to employ interpolation methods to properly evaluate the Lagrangian time derivatives for each component. Such methods have previously been implemented for 1D CPWM numerical algorithms,[33] and have also been carried out for 1D problems involving multiple diabatic potential surfaces.[34] Certainly this scheme is a viable approach here and we note that this would offer much greater control over the time step and accuracy of the BRPH calculations. However, the interpolation codes are somewhat awkward to work with and create some extra computational overhead. At the present stage of development we have avoided the interpolation issue by using a unique time step for each channel

$$\Delta t_i = \frac{\Delta x}{v_i} = \Delta x\sqrt{\frac{m}{2(E - E_i)}} \tag{38}$$

so that the + (or −) BRPH grid points associated with the different channels will be coincident with one another after each time step. This choice automatically yields imaginary time steps for the closed channel amplitudes. Of course, this then implies that the solutions will not be coincident with respect to time, and we will come back to this important point momentarily. For individual time steps, we employ a second-order Runge−Kutta integration scheme,[55] where the BRPH solutions are propagated using the formula

$$a_{i\pm}(x \pm \Delta x, t + \Delta t_i) = a_{i\pm}(x,t) + K^{(2)}_{i\pm} \tag{39}$$

where

$$K^{(1)}_{i\pm} = \Delta t_i \mathrm{d}_t(a_{i\pm}(x,t)) \tag{40a}$$

$$K^{(2)}_{i\pm} = \Delta t_i \mathrm{d}_t(a_{i\pm}(x,t) + K^{(1)}_{i\pm}/2) \tag{40b}$$

The factor enclosed by parentheses in eq 40b represents a first-order half-step, i.e., $\Delta t_i/2$, while eq 39 is the second-order full-step. The error for each Runge−Kutta step is third-order in $|\Delta t_i|$, which is different for different channel amplitudes, and the cumulative error is second-order.

Note that in the application of eqs 39 and 40 we must take care of the fact that ± grid points at the half-step will be offset from one another. This can be efficiently handled by applying a shift function, as necessary, to evaluate all of the $\Phi_{i\pm}$ components at the same point in space. For example, consider a discrete numerical representation of the channel scattering amplitudes:

$$a_{i\pm}(t) = \{a_{i\pm}(x_1), \ldots, a_{i\pm}(x_{k-1}), a_{i\pm}(x_k), a_{i\pm}(x_{k+1}), \ldots, a_{i\pm}(x_N)\} \tag{41}$$

where the set of points $\{x_1, ..., x_N\}$ are the numerical grid points along the reaction coordinate. Note that $x_{i+1} = x_i + \Delta x$, so that after a full first-order time step Δt_i, the components will be given by

$$a_{i+}(t + \Delta t_i) = \{a_{i+}(x_2), ..., a_{i+}(x_k), a_{i+}(x_{k+1}), a_{i+}(x_{k+2}), ..., a_{i+}(x_{N+1})\} \quad (42a)$$

$$a_{i-}(t + \Delta t_i) = \{a_{i-}(x_0), ..., a_{i-}(x_{k-2}), a_{i-}(x_{k-1}), a_{i-}(x_k), ..., a_{i-}(x_{N-1})\} \quad (42b)$$

where it is clear that $a_{i\pm}$ components are not properly aligned with one another in space. Equation 42 is also valid for first-order half-steps provided that we make the replacement $x_i \rightarrow x'_i = x_i + \Delta x/2$. To evaluate the time derivative of the components for the next time step, the $\pm$ components need to be calculated at the same point in space, so we apply a pair of shift functions that yield

$$\text{Shift}_+[a_{i+}(t + \Delta t_i)] = \{a_{i+}(x_{N+1}), ..., a_{i+}(x_{k-1}), a_{i+}(x_k), a_{i+}(x_{k+1}), ..., a_{i+}(x_N)\} \quad (43a)$$

$$\text{Shift}_-[a_{i-}(t + \Delta t_i)] = \{a_{i-}(x_1), ..., a_{i-}(x_{k-1}), a_{i-}(x_k), a_{i-}(x_{k+1}), ..., a_{i-}(x_0)\} \quad (43b)$$

Here the interior positions are now coincident in space and the points at the edges of the BRPH grid are meaningless and potentially dangerous. This is not a problem, however, because between time steps the edge points are replaced with the appropriate boundary conditions for the desired solutions

$$a_{i+}(t + \Delta t_i) = \{e^{i/\hbar(p_i x_1 - E\Delta t_i)}, ..., a_{i+}(x_{k-1}), a_{i+}(x_k), a_{i+}(x_{k+1}), ..., a_{i+}(x_N)\} \quad (44a)$$

$$a_{i-}(t + \Delta t_i) = \{a_{i-}(x_1), ..., a_{i-}(x_{k-1}), a_{i-}(x_k), a_{i-}(x_{k+1}), ..., 0\} \quad (44b)$$

These shifts are applied after both the half and full time step so that the BRPH solutions are always coincident in space, thus eliminating the need for interpolation schemes.

Certainly, the mismatch in the treatment of time between different scattering amplitudes is somewhat counterintuitive and warrants some concern. To justify this, we must recognize that the time-dependent dynamics encapsulated by both the CPWM and BRPH equations do not represent the actual physical dynamics in the deterministic sense. By this we mean that the BRPH solutions at intermediate times have no physical importance apart from the fact that the (exact FF solution) bipolar components possess a dynamic phase factor, $e^{-iEt/\hbar}$, that is consistent with the true stationary state. However, this time dependence is clearly known *a priori*, and the value of t is completely arbitrary for stationary states. In our numerical applications we have often found that it is useful to reset the phase of the CPWM or BRPH solutions between time steps Δt_i by applying a conjugate phase factor of $e^{+iE\Delta t_i/\hbar}$. This works for both real and imaginary time steps and has no consequential effect in the long-time limit, changing only the intermediate-time dynamics, which are unimportant. Thus, neither the precise form of the initial conditions for the BRPH propagation nor the slight phase shifts between time-steps as discussed above prevent the method from reaching the desired steady-state solution in the long-time limit, at least not in principle.

That said, CPWM algorithms are somewhat similar to numerical optimization problems, such as the Newton−Raphson method, or other iterative methods for self-consistently solving nonlinear equations, like the Hartree−Fock equations. Nonconvergent, or worse yet divergent, solutions will often occur when the initial guess is too far removed, or perhaps even completely isolated (in solution space) from the desired solution. We have observed similar behavior in some BRPH calculations, especially for energies very close to the onset of a scattering channel. From experience, we expect to encounter difficulties with convergence when the quantities $E - E_i$ are small and the troublesome scattering amplitude has a very broad de Broglie wavelength compared to the other components and the size of the interaction region. Related issues are also encountered in 1D applications, as the kinetic energy approaches zero. The obvious solution is to add points to the numerical grid. Ideally it would be desirable to have enough grid points outside the interaction region to guarantee that $\varepsilon_i(x)$ and the adiabatic couplings are numerically converged. At the same time, the grid spacing must be chosen to accurately represent the scattering potential. At some point, usually when the energy is an extremely small fraction of the barrier height, one cannot afford to add enough points to maintain an adequate representation of both the potential and the scattering state simultaneously. For multi-D calculations, the problem is more serious because the same issues will occur over an energy range where the **S**-matrix elements are nontrivial and do exhibit interesting features. Note that this situation is not unique to BRPH and is, in fact, problematic for virtually all accurate quantum scattering methods (especially DVR-ABC). In any case, it is clear that, like the 1D case, the BRPH will ultimately fail for some small enough value of $E - E_i$; however, we would like to be able to push the method as far as possible.

In this context, there are several avenues that could lead to enhanced numerical stability. One idea is to take the final BRPH components from a presumably stable calculation at higher energy and use these as the initial conditions for lower kinetic energies, where stability is problematic. To compute the **S**-matrix as a function of energy, one would scan the energy backward from higher to lower values. We could also mix different solutions from completed calculations above and below the channel onset. Another approach may be to slowly "switch on" the nonadiabatic coupling terms with an appropriately defined scaling factor. In our work we have employed a very simple formula

$$a_{i\pm}(\text{new}) = a_{i\pm}(\text{old}, t) + \eta[a_{i\pm}(\text{old}, t + \Delta t_i) - a_{i\pm}(\text{old}, t)] \quad (45)$$

which mixes the BRPH solutions between time steps, and the mixing parameter η is a number between (0,1).[56] We have found that this does enhance numerical stability for some cases, but ultimately fails as the energy gets even closer to the onset of a scattering channel.

4. RESULTS

In this section we present benchmark BRPH results for several simple 2D scattering problems. The first example involves the trivial case of a separable system defined by an Eckart barrier along x and a harmonic oscillator (HO) along y. We refer to this system as the uncoupled Eckart+HO problem. Since there is no coupling between x and y, the adiabatic eigenfunctions are constant with respect to the reaction coordinate, such that the

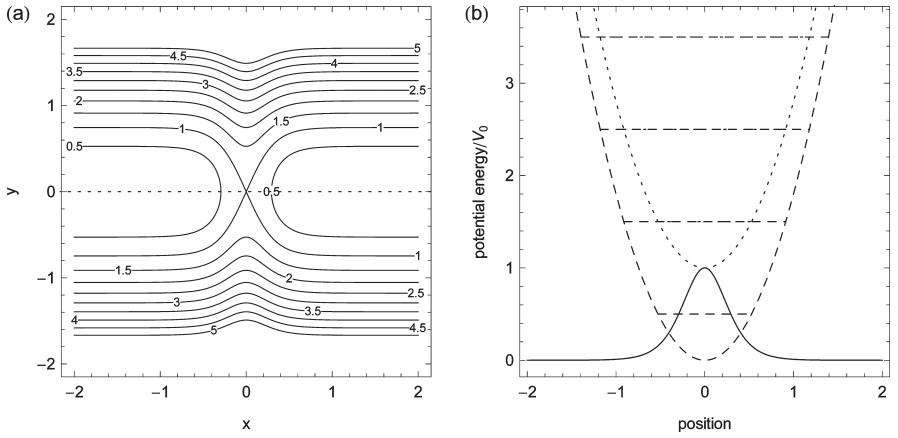

Figure 3. (a) Contour lines illustrating the 2D potential energy surface for the uncoupled Eckart+HO problem. The isovalues are reported in units of the barrier height V_0 = 0.0018 hartree. The dotted line corresponds to the minimum energy path. (b) Various 1D slices through the potential energy surface are shown. The solid curve illustrates the Eckart barrier along the linear reaction path $V(x,0)$. The dashed curves correspond to the asymptotic harmonic oscillator potential $V(\pm\infty,y)$ and its four lowest energy eigenvalues. The dotted curves are associated with the harmonic potential and eigenvalues along the dividing surface $V(0,y)$.

nonadiabatic coupling terms vanish and the interchannel reaction probabilities $P_{n\to i\neq n} = 0$ for all energies. Our results here will serve as a reference for a nonseparable problem that we consider later. The scattering potential for the uncoupled Eckart+HO problem is given by

$$V(x,y) = V_0 \operatorname{sech}^2(\alpha x) + \frac{1}{2} m\omega_0{}^2 y^2 \tag{46}$$

where the parameters of the problem are given as follows: m = 2000 au, $V_0 = \hbar\omega_0$ = 0.0018 hartree, and α = 3 b^{-1}. Diagrams illustrating the 2D structure and various 1D slices of the scattering potential are shown in Figure 3.

In Figure 4 we plot 1D probability densities for the channel scattering square amplitudes, $\rho_i = |a_i|^2$, and corresponding BRPH components, $\rho_{i\pm} = |a_{i\pm}|^2$, for the two degenerate left-incident stationary scattering state solutions of the uncoupled Eckart+HO problem with energy $E = 2V_0$. In each case, only a single channel is involved, i.e., the incident channel, $i = n$, because there is no nonadiabatic coupling. These functions are quite similar to the 1D example in section 2, except that there are multiple solutions to consider when there is more than one open scattering channel. Panels a and b show the densities for the $n = 0$ and $n = 1$ incident states, respectively. Clearly, the $n = 0$ state has a larger kinetic energy and the scattering amplitude exhibits a shorter wavelength and greater transmission than the $n = 1$ state.

The BRPH components and scattering amplitudes can be combined with the adiabatic eigenfunctions to generate 2D wave functions and probability densities:

$$\rho_+(x,y) = \left| \sum_i a_{i+}(x)\, \phi_i(x,y) \right|^2 \tag{47a}$$

$$\rho_-(x,y) = \left| \sum_i a_{i-}(x)\, \phi_i(x,y) \right|^2 \tag{47b}$$

$$\rho(x,y) = \left| \sum_i a_i(x)\, \phi_i(x,y) \right|^2 \tag{47c}$$

where ρ_+ represents the density of the total incident and transmitted wave, ρ_- is the density of the total reflected wave, and ρ is the total probability density of the stationary state. In Figure 5, we plot these densities for the two degenerate left-incident states at $E = 2V_0$. Because there is no interference between channels in this case, the wave functions involved are simply the product of a single 1D scattering wave function (single-channel scattering amplitude) and an HO eigenfunction. Consequently, these densities are not particularly interesting for the uncoupled case; however, they do serve as a useful point of reference.

For the uncoupled Eckart+HO problem, the intrachannel reaction probabilities are identical to the transmission probability for the 1D Eckart barrier. In Figure 6a we plot the intrachannel reaction probabilities $P_{n\to n}$ as a function of energy for the first three scattering channels with $E < 3.5V_0$. The calculated values for the $n = 0$, 1, and 2 channels are represented by circles, squares, and diamonds, respectively. The vertical dashed lines in the figure indicate the onset of a scattering channel, i.e., $E = E_i$, and the exact results are shown as solid lines. We have calculated these results for several different grid spacings; however, only the most accurate results using Δx = 0.0025 b are presented. Figure 6b shows the fractional error of the BRPH transmission probabilities. These errors are all less than 0.1% across the energy range and are quite similar compared to those for the 1D case; however, for the 2D problem, we have degenerate states at higher energies, and a separate error is given for each one. Generally, the error is larger for states where the kinetic energy is small and the time step is large. We note the anomalously low error in the data point for the $n = 2$ channel at $E = 2.6\ V_0$. This is the most challenging state for this set of calculations, and we suspect that there may be a small unconverged error leading to a coincidental cancellation in favor of a seemingly more accurate transmission probability.

The error estimates introduced in section 2 for CPWM calculations can also be generalized for BRPH calculations. In panels c and d of Figure 6 we plot the normalization error and $\langle \hat{H} \rangle_{\text{error}}$, respectively. For multi-D problems, we define the normalization as the sum of the partially state resolved transmission and reflectance probabilities, which should be unity for all open channels. The magnitude of both the normalization and energy expectation errors is less than 0.1% across the given energy range and exhibit similar trends with respect to the grid spacing (not shown) as

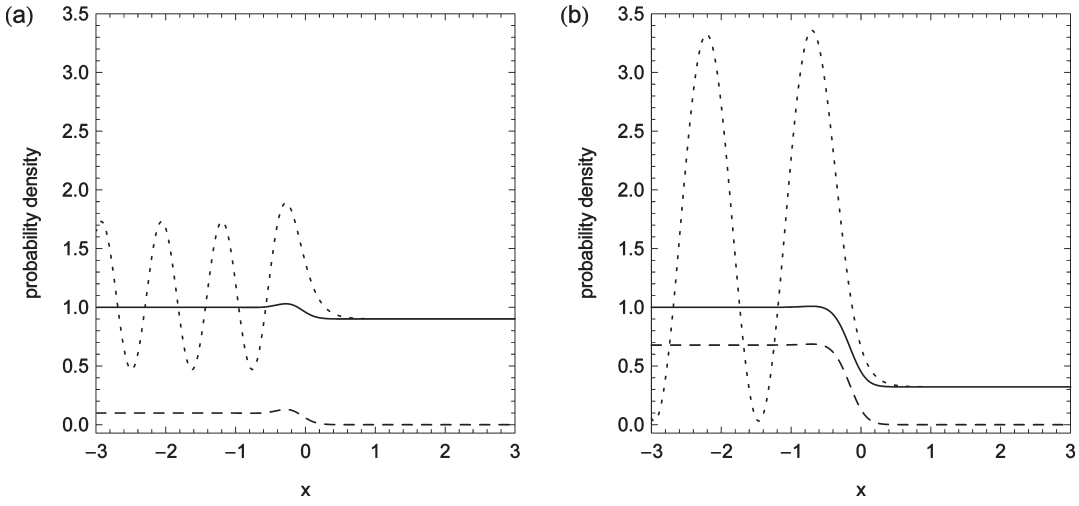

Figure 4. The BRPH densities for two degenerate stationary states of the uncoupled Eckart+HO problem are plotted as a function of the reaction coordinate: (solid) ρ_{n+}, (dashed) ρ_{n-}, and (dotted) ρ_n. These states correspond to the two open scattering channels with $E = 2V_0$. Panels a and b correspond to the $n = 0$ and $n = 1$ incident channels, respectively.

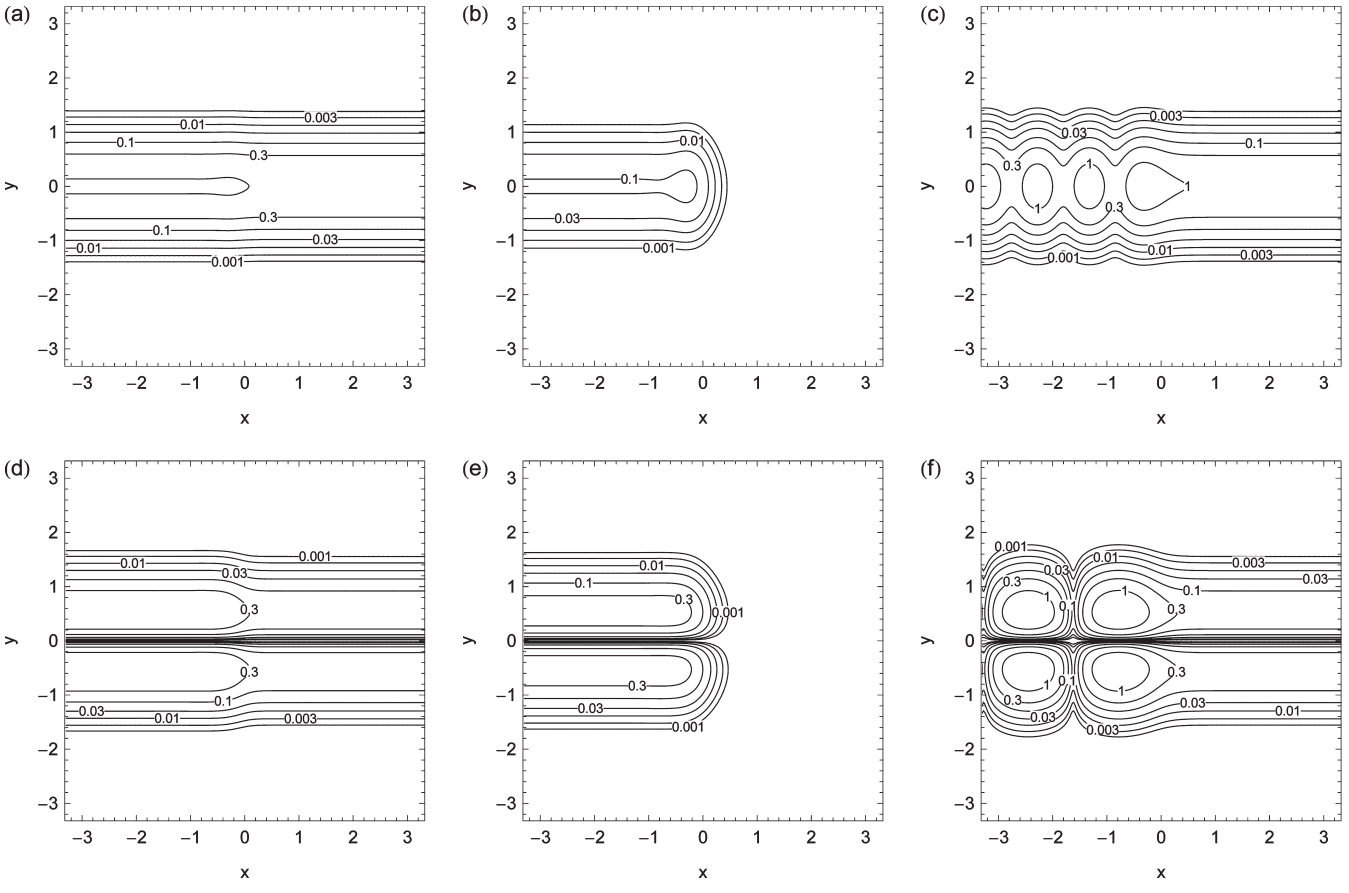

Figure 5. Contour plots illustrating 2D BRPH densities for the two degenerate stationary states of the uncoupled Eckart+HO problem with $E = 2V_0$. For the $n = 0$ incident channel, we have (a) ρ_+, (b) ρ_-, and (c) ρ. Similarly, panels d−f are the corresponding densities for the $n = 1$ incident channel.

compared to the CPWM results for the 1D Eckart A problem. Interestingly, however, the energy dependence of the these errors is quite different compared to the errors shown in Figure 2. For the 1D problem, the errors increase regularly with energy, whereas in panels c and d of Figure 6 they generally decrease, although, the errors for the $n = 0$ incident channel do increase with energy, but only after the total energy has exceeded the $n = 1$ channel onset. We speculate that the difference between the multi-D and 1D errors is related to the fact that the BRPH equations of motion contain constant terms, i.e., E_i, that are not present in the 1D CPWM equations. Certainly this is an interesting, although very subtle, feature of our results that we will continue

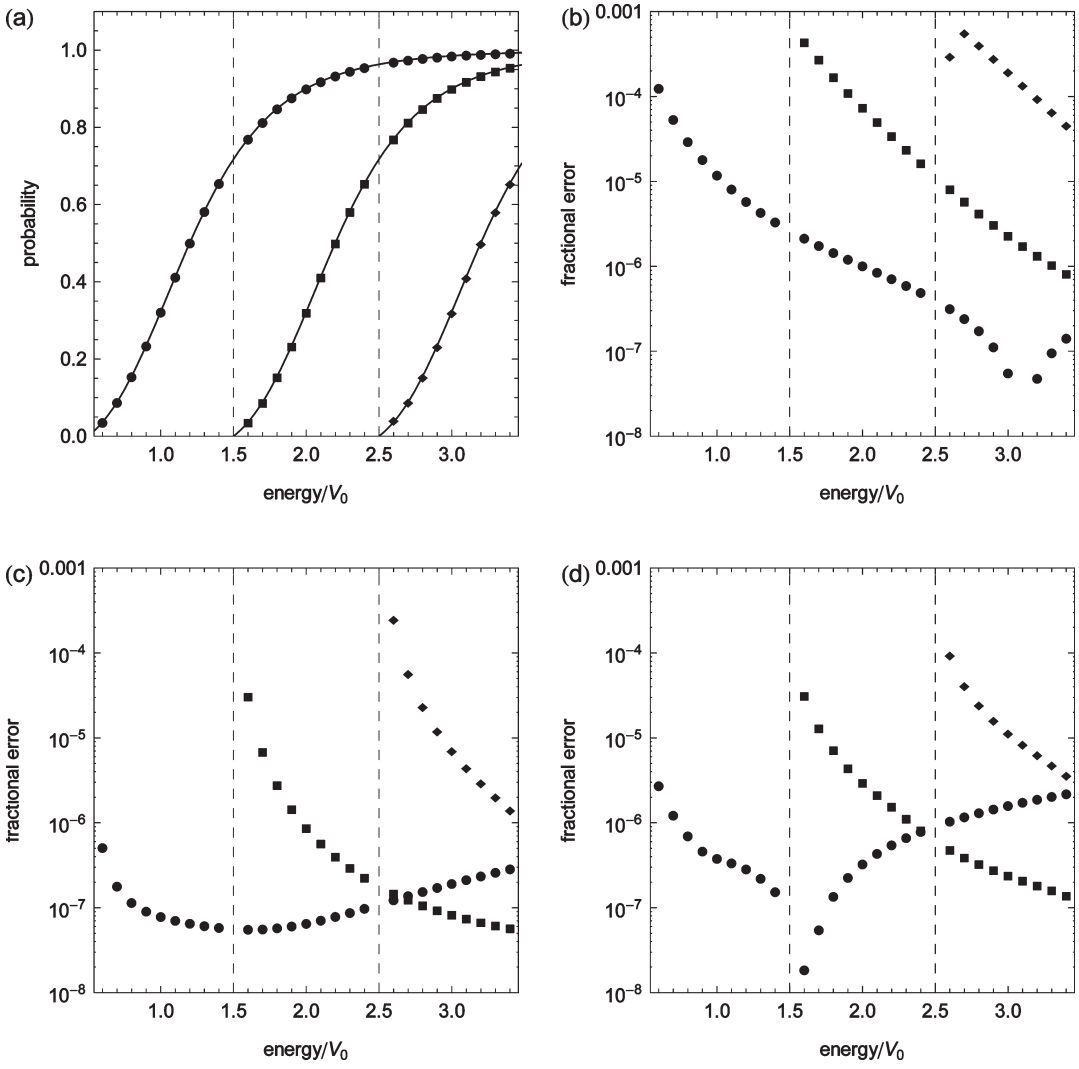

Figure 6. Transmission probabilities and fractional error estimates as a function of energy in units of the barrier height $V_0 = 0.0018$ hartree for the uncoupled Eckart+HO problem. Circles, squares, and diamonds represent the $n = 0$, 1, and 2 incident channels, respectively. Vertical dashed lines indicate the onset of a scattering channel. (a) Intrachannel transmission probabilities; solid lines are the corresponding exact results. (b) Fractional error in the calculated transmission probabilities. (c) Fractional error of the normalization condition for the 2D stationary states. (d) Fractional error in the energy expectation value of the stationary states.

to examine in future studies; however, the important point here is that BRPH approach reproduces analytical results extremely well for this uncoupled problem and that the error can be controllably reduced to arbitrary precision by decreasing the grid spacing.

In the next example, we a consider a coupled Eckart+HO problem where the harmonic oscillator potential is displaced along the reaction coordinate. The potential energy surface is defined by

$$V(x,y) = V_0 \operatorname{sech}^2(\alpha x) + \frac{1}{2} m\omega_0{}^2 (y - Y(x))^2 \qquad (48)$$

where the function

$$Y(x) = Y_0 \operatorname{sech}^2(\alpha x) \qquad (49)$$

provides a displacement that couples motion along the x and y coordinates. The displacement is zero as $x \to \pm\infty$ and has a maximum value of $Y_0 = 0.25$ b at the dividing surface $x = 0$. In principle, we could use this curve to define the reaction coordinate; however, this is not necessarily required because the reactant and product valleys of the potential are coincident with the x-axis. In this sense, the problem is quasilinear and we will take the x-axis to be the reaction coordinate in our calculations. The other parameters of the coupled problem are identical to those in the uncoupled Eckart +HO example. Figure 7 shows the 2D potential energy surface and several 1D slices for the coupled Eckart+HO problem.

The fact that we have included a displacement of the oscillator, as opposed to varying only the harmonic frequency along the reaction coordinate, is important. In the case of the coupled Eckart+HO with no displacement[35,57] (i.e., symmetric about y), the nonadiabatic coupling between even and odd adiabatic eigenstates vanishes due to symmetry, and one would need to probe higher energies in order to observe nonzero state-to-state transitions. However, the intrachannel reaction probabilities at high energies will far outweigh the interchannel probabilities for the symmetric Eckart+HO problem, i.e., $P_{0\to0} \approx 1 \gg P_{0\to2}$, which makes it difficult to assess whether the nonadiabatic coupling terms are treated correctly. Breaking the symmetry of the problem by simply displacing the oscillator leads to much more obvious and interesting nonadiabatic effects at lower energies, even without

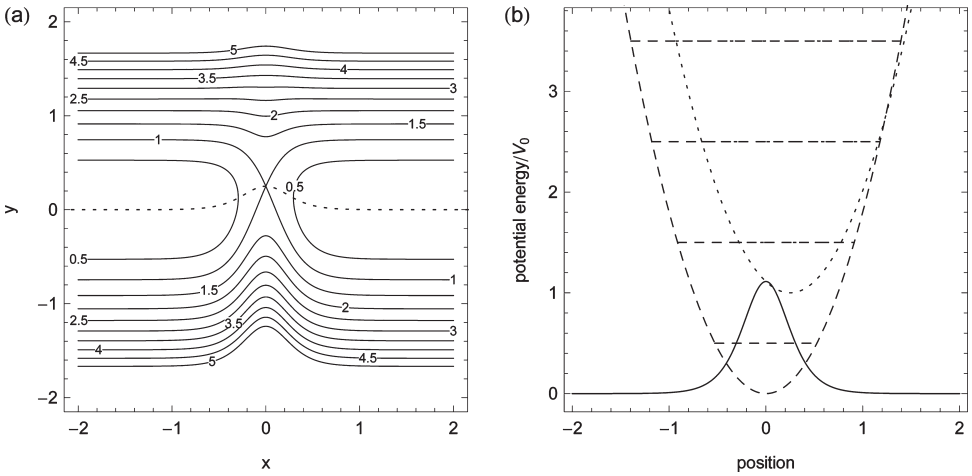

Figure 7. (a) Contour lines illustrating the coupled Eckart+HO potential. The isovalues are reported in units of the barrier height $V_0 = 0.0018$ hartree. The dotted line corresponds to the minimum energy path. (b) Various 1D slices of the 2D potential are shown. The solid curve illustrates $V(x,0)$. The dashed curves correspond to $V(\pm\infty,y)$ and the four lowest energy asymptotic eigenvalues E_i. The dotted curves represent $V(0,y)$ and the four lowest adiabatic eigenenergies $\varepsilon_i(0)$. The maximum displacement of the oscillator is 0.25 b at the dividing surface.

attenuating the harmonic frequency. In Appendix B we derive expressions for the nonadiabatic BRPH integrals (eq 29) for the case where the harmonic oscillator is both displaced and scaled along the reaction coordinate. For the displaced only oscillator, we have the following result

$$I_{ij}^{(1)} = -\sqrt{2}\beta Y'\sqrt{(i+1)}\delta_{i,j-1} + \sqrt{2}\beta Y'\sqrt{i}\delta_{i,j+1} \quad (50a)$$

$$I_{ij}^{(0)} = \frac{1}{2}\beta^2 Y'^2(\sqrt{(i+2)(i+1)}\delta_{i,j-2} + \sqrt{i(i-1)}\delta_{i,j+2}) - \frac{\sqrt{2}}{2}\beta Y''(\sqrt{(i+1)}\delta_{i,j-1} - \sqrt{i}\delta_{i,j+1}) - \frac{1}{2}\beta^2 Y'^2(2i+1)\delta_{i,j} \quad (50b)$$

where $\beta = (m\omega_0/\hbar)^{1/2}$. These terms introduce coupling between specific scattering channel amplitudes, and the magnitude of this coupling is scaled by functions of the reaction coordinate that depend on the derivatives of Y.

We have calculated the stationary states and reaction probabilities for the coupled Eckart+HO problem over a range of energies that includes up to three open scattering channels. Recall that the BRPH ansatz (eq 20) involves an infinite sum over both the open and closed scattering channels and that for coupled problems this sum must be artificially truncated. We have performed calculations including up to three additional closed channel amplitudes, and we found that with inclusion of only two closed channel terms, the accuracy in the results shown below is limited by the grid spacing, which is $\Delta x = 0.0025$ b for our most accurate BRPH calculations. This is certainly not a general result, and we expect that more terms will be required to achieve convergence for different types of scattering problems, especially those with significant nonadiabatic coupling and also anharmonic character in the perpendicular degrees of freedom.

Figure 8 shows the BRPH densities as a function of x for the two degenerate left-incident stationary state solutions with energy $E = 2V_0$. In each panel, the solid line corresponds to a ρ_{i+} density, the dashed line to ρ_{i-}, and the dotted line to ρ_i. Panels a and d show the incident channel densities corresponding to the $n = 0$ and $n = 1$ incident channel stationary states, respectively. Qualitatively, the curves are very similar to the uncoupled case; however, the intrachannel transmission is decreased. The densities shown in panels b and e are associated, respectively, with the nonincident channels corresponding to panels a and d; these would be formally zero if the problem were uncoupled. Thus, Figure 8b illustrates the $\rho_{1\pm}$ and ρ_1 densities for the $n = 0$ incident state, and similarly, Figure 8d shows the $\rho_{0\pm}$ and ρ_0 densities for the $n = 1$ incident state. In both cases $\rho_{i\neq n\pm} \rightarrow 0$ as $x \rightarrow \mp\infty$, which is consistent with the required boundary conditions. Panels c and f show the closed channel densities $\rho_{2\pm}$ and ρ_2 for the $n = 0$ and $n = 1$ incident states, respectively. For both cases, the closed channel densities all vanish as $x \rightarrow \pm\infty$, so that there is no net transmission or reflectance probability associated with the closed channel. While the magnitude of the closed channel densities are smaller compared to the open channels, they are clearly not negligible. The 2D densities $\rho_\pm$ and ρ for the degenerate states with $E = 2V_0$ are shown in Figure 9. The patterns are similar to those for the uncoupled case; however, there are distortions attributed to the nonadiabatic coupling between scattering amplitudes. This is most clearly seen in Figure 9c, where the irregularities in the total ρ indicate the presence of nontrivial interference effects.

As we have discussed previously, the asymptotic values of the open channel ρ_{j+} as $x \rightarrow \infty$ for a given left-incident channel n are related to the state-to-state transmission probabilities $P_{n\rightarrow j}$. Also, the cumulative reaction probability is given by the sum

$$N(E) = \sum_{n,j} P_{n\rightarrow j}(E) \quad (51)$$

In Figure 10 we compare the calculated BRPH reaction probabilities with those obtained using the DVR-ABC method.[12−14,54] See Appendix C for a discussion of the latter calculations. Figure 10a shows the state-to-state probabilities for the coupled Eckart+HO problem on a logarithmic scale as a function of energy. Note that the energy scale here is measured in units of the barrier height V_0 and that the vertical dashed lines indicate the onset of a scattering channel. The BRPH probabilities for individual transitions $n \rightarrow j$ are given by circles, squares, etc. and the corresponding DVR-ABC results are indicated with the symbol $\times$ for all transitions. At low energies, only the ground state $(n = 0)$ scattering channel is open. The BRPH $0 \rightarrow 0$ transmission probabilities are represented by filled circles, and these increase more or less steadily across the given energy range; however, there

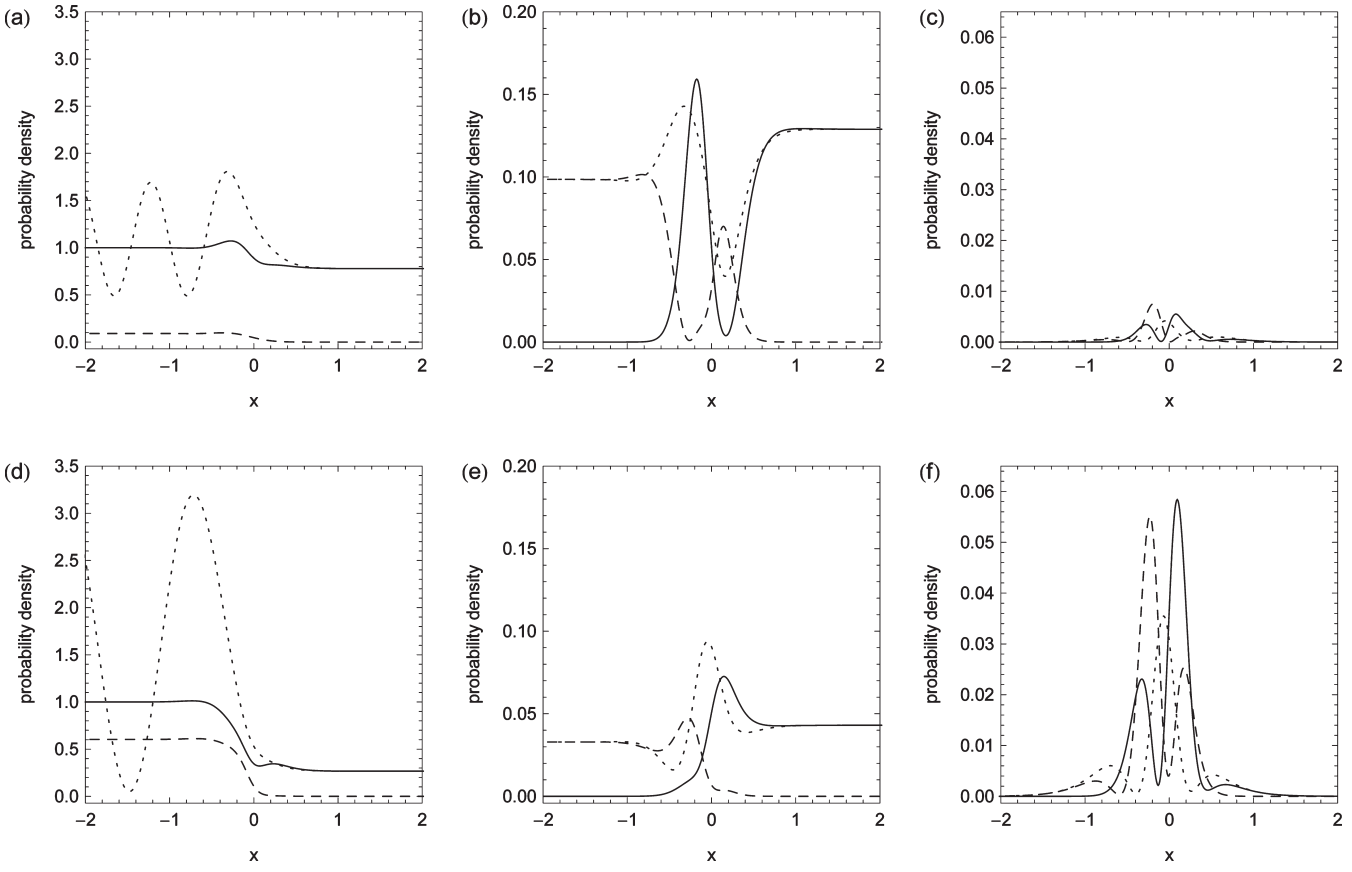

Figure 8. BRPH densities as a function of x for two degenerate ($E = 2V_0$) left-incident stationary states of the coupled Eckart+HO problem: (solid) ρ_{i+}, (dashed) ρ_{i-}, and (dotted) ρ_i. Panels a and d show the intrachannel densities for the $n = 0$ and $n = 1$ incident scattering channels, respectively, while panels b and e show the nonincident channel densities, i.e., $i = 1$ and $i = 0$, respectively. Panels c and f are the closed channel $i = 2$ scattering amplitudes contributing to the $n = 0$ and $n = 1$ incident channels, respectively.

are subtle variations at higher energies, where interstate transitions occur. The $1 \rightarrow 1$ and $2 \rightarrow 2$ transmission probabilities are depicted as up-triangles and empty circles, respectively. These are qualitatively similar to the $0 \rightarrow 0$ transmission, although the variation at higher energies is visibly larger for the $1 \rightarrow 1$ transmission probability compared to the $0 \rightarrow 0$ case. This makes sense in light of the fact that the scaling factors in eq 50 are proportional to the incident state quantum number and the fact that the $n = 0$ incident state can only couple to higher energy scattering states, whereas the $n = 1$ incident state is coupled to higher and lower energy states. The filled squares, diamonds, and down-triangles in Figure 10a represent the $0 \rightarrow 1$, $0 \rightarrow 2$, and $1 \rightarrow 2$ transmission probabilities, respectively. These begin to increase after the onset of their respective scattering channels. The $0 \rightarrow 1$ and $0 \rightarrow 2$ transmission probabilities are observed to decrease with increasing energy, and we speculate the same behavior would also be observed for $1 \rightarrow 2$ at higher energies.

Figure 10a shows that there is very good qualitative agreement between the BRPH and DVR-ABC calculations. In Figure 10b we plot the fractional (or relative) differences between the BRPH and DVR-ABC transmission probabilities, which are calculated according to the formula

$$\text{fractional difference} = \frac{2|P_{\text{BRPH}} - P_{\text{DVR}}|}{|P_{\text{BRPH}}| + |P_{\text{DVR}}|} \tag{52}$$

Panel b illustrates that the two sets of calculations are also, generally, quantitatively consistent with one other across the given energy range. Note that the largest differences, roughly 1% and 5%, are found for the two energy values just above the channel thresholds at $E = 1.5V_0$ and $E = 2.5V_0$, respectively. For reasons that we have discussed previously, it is difficult to obtain convergence for states with very low kinetic energies, and we attribute the larger differences here to this issue, which affects the accuracy in both the BRPH and DVR-ABC methods. Figure 10c compares the cumulative reaction probability as a function of energy for our BRPH and DVR-ABC calculations. Qualitatively speaking, the agreement is excellent, and Figure 10d examines the fractional differences between the two methods. Generally, the differences are all much less than 0.1% over the given energy range with the exception of just above the channel thresholds, where they are roughly equal to 0.1%; i.e., there are at least two significant figures in common, which is still fairly good. The convergence of the cumulative reaction probability with respect to the grid parameters in our DVR calculations has been monitored closely, and the differences here between the BRPH and DVR-ABC results are of the same order of magnitude as the individual convergence in these numbers with respect to the BRPH and DVR grid parameters; hence, we can conclude that the two methods are quantitatively consistent with one another.

As an independent assessment of the BRPH performance, we also examine the fractional errors in the normalization and energy

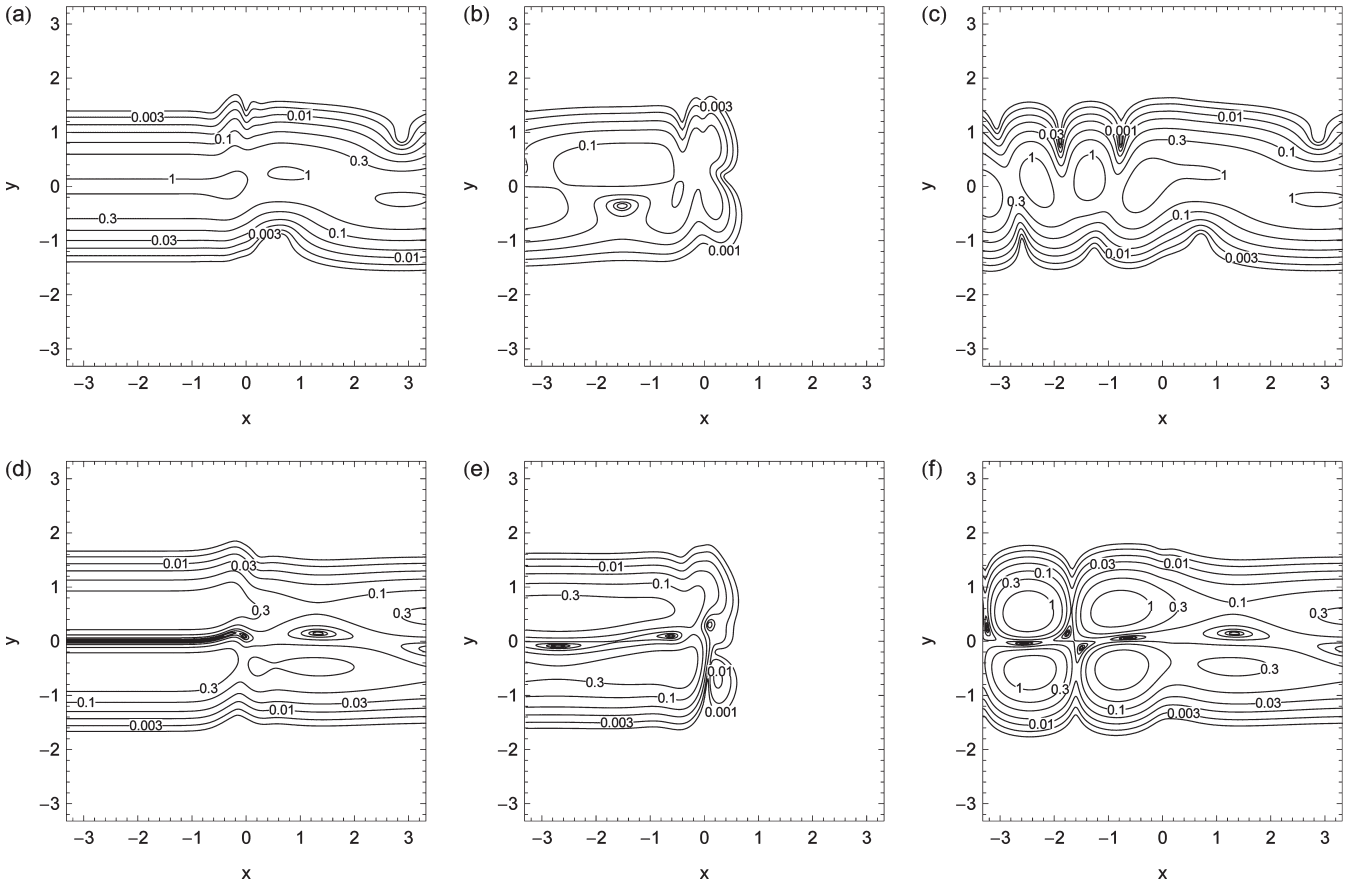

Figure 9. Contour plots illustrating 2D BRPH densities for the two degenerate stationary states ($E = 2V_0$) of the coupled Eckart+HO problem. For the $n = 0$ incident states, we have (a) ρ_+, (b) ρ_-, and (c) ρ. Similarly, panels d−f are the corresponding densities for the $n = 1$ incident state.

expectation value, which are plotted in panels a and b of Figure 11, respectively. Here each incident channel has its own error measure and there are up to three channels for the highest energy values shown. Generally, the errors for the coupled problem are comparable to those for the uncoupled Eckart+HO potential; however, the energy dependence is qualitatively distinct. Of course, we should expect some differences between the uncoupled and coupled problems; the latter are nontrivial and it is reasonable to expect larger errors. In any case, both fractional error measures are less than 0.1% across the given energy range, so that we may conclude the BRPH solutions for the coupled problem are also quantitatively consistent with both the normalization requirements of the stationary states and the TISE.

Taken together, the differences and errors shown in Figures 10 and 11, respectively, suggest that the BRPH results are likely more accurate than the DVR-ABC calculations at the energies just above the scattering channel thresholds. One concrete indication of this is that the energy expectation errors shown in Figure 11b are on the order of 10^{-4} or better across the energy range; however, the consistency between the BRPH and DVR-ABC calculations is only 10^{-2} in the state-to-state probabilities near the channel threshold and 10^{-4} or better away from threshold (see Figure 10b). As discussed in Appendix C, the discrepancy can be attributed to the fact that we could not fully converge our DVR-ABC calculations with respect to the size and density of the DVR grid at the energies just above the thresholds. This suggests that the BRPH approach may offer a computational advantage over the DVR-ABC method for calculating reaction probabilities at near-threshold energies. The time complexity for both the DVR-ABC and BRPH approaches scales as $O(N^3)$, where N is the total number of grid points used in the calculations. For DVR-ABC, the value of N required to achieve a certain level of precision increases as the total energy gets closer to a channel threshold, while for the BRPH, the precision is more or less constant with respect to energy for a fixed N, assuming a fixed number of scattering channels. This issue also affects the memory requirements of the two methods, and it seems that BRPH has an advantage near a channel threshold. We intend to continue exploring these issues in future work.

5. BRIEF SUMMARY AND OUTLOOK

In this work we have described the development of a computational methodology, the BRPH approach, for the calculation of multi-D stationary scattering state wave functions and reaction probabilities in reactive scattering problems. We have presented benchmark results for the simplest class of 2D scattering problems with linear reaction coordinates. The BRPH approach utilizes an adiabatic representation of the system's Hamiltonian to recast the multi-D problem into a set of coupled 1D scattering problems, and we can then exploit the same numerical algorithms used in 1D CPWM applications to calculate the stationary states and state-to-state reaction probabilities of 2D problems. In our numerical applications, we have demonstrated that BRPH calculations are both qualitatively and quantitatively consistent with conventional methods based upon the DVR-ABC approach. Importantly, the BRPH method does not require the use of ABCs

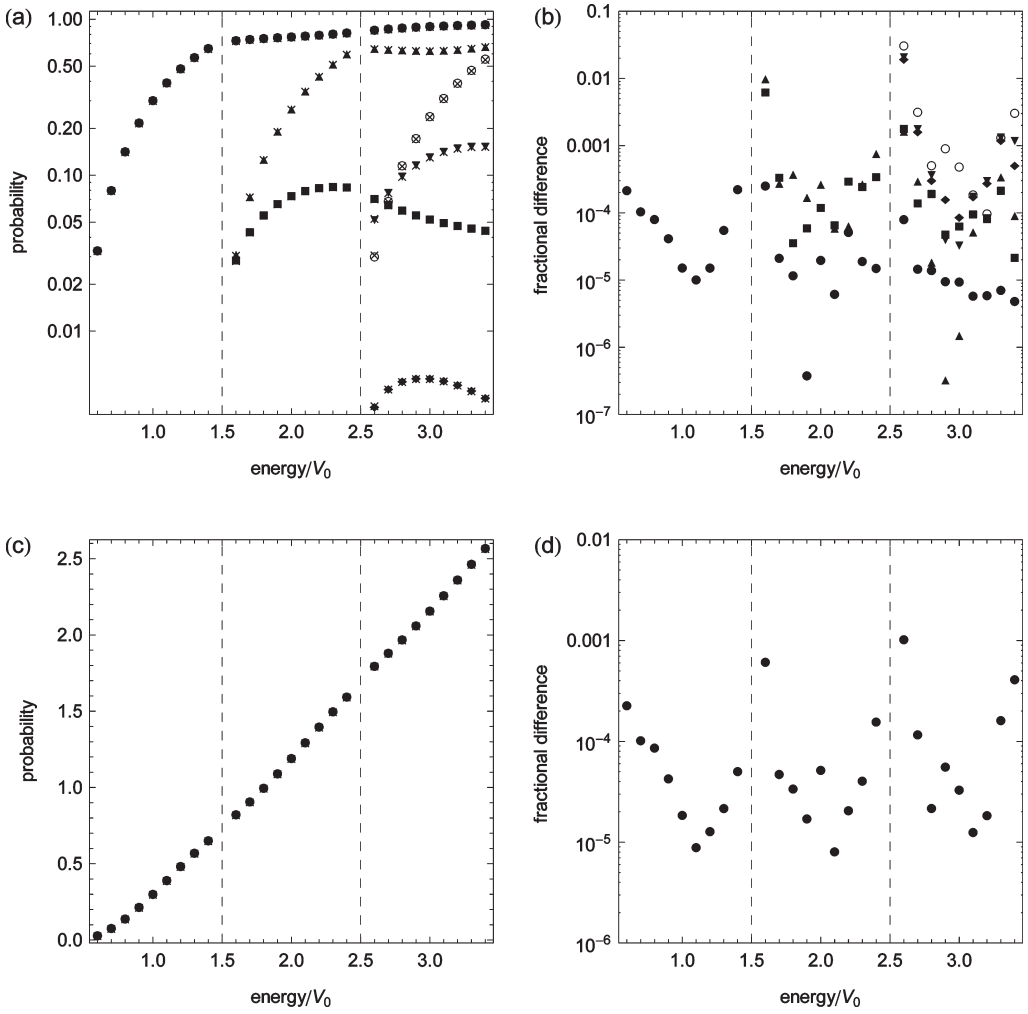

Figure 10. Reaction probabilities and fractional differences as a function of energy in units of the barrier height $V_0 = 0.0018$ for the coupled Eckart+HO problem. Vertical lines represent the onset of a scattering channel. (a) The BRPH state-to-state transmission probabilities are represented as follows: (filled circles) $0 \rightarrow 0$, (squares) $0 \rightarrow 1$, (diamonds) $0 \rightarrow 2$, (up-triangles) $1 \rightarrow 1$, (down-triangles) $1 \rightarrow 2$, and (empty circles) $2 \rightarrow 2$. The corresponding DVR-ABC transmission probabilities are represented with the symbol $\times$ for all probabilities. (b) Fractional differences between the BRPH and DVR-ABC state-to-state reaction probabilities. The differences for the various probabilities are represented according to the same scheme used in panel a for the BRPH probabilities. (c) Comparison of (circles) BRPH and ($\times$) DVR-ABC cumulative reaction probabilities. (d) Fractional difference between the BRPH and DVR-ABC cumulative reaction probabilities.

so that the range of the computational grid needed in BRPH calculations is much smaller than that for DVR-ABC.

In future work, we plan to extend the theoretical and numerical implementation of the BRPH approach to include asymptotically asymmetric potentials, larger dimensionalities, and curvilinear reaction paths. Asymptotically asymmetric problems do not really present a major challenge, since we can exploit techniques developed in previous work for dealing with such problems.[33] Curvilinear reaction paths and higher dimensionalities, on the other hand, present a much more interesting and challenging class of problems. To address the issue of curvature, in 2D for example, we speculate that the BRPH approach could be applied within a set of orthogonal natural collision coordinates $s = s(x,y)$ and $q = q(x,y)$, where the channel scattering amplitudes $a_i(s)$ would be defined along some curved reaction path, which is a function of MWC coordinates x and y. Likewise, the adiabatic eigenfunctions would vary as $\phi_i(s,q)$, where q is associated with bound motion perpendicular to the reaction coordinate, e.g., a bead oscillating along a curved wire. Generally, the kinetic energy operator expressed in terms of s and q will not have a simple form, so we expect that the adiabatic eigensystem will have to be represented numerically (possibly with 1D DVRs for bound states) in order to obtain exact results. It is also expected that the BRPH integrals will depend upon the metric tensor for the curvilinear coordinate system, and the BRPH equations of motion and the nonadiabatic coupling terms will be correspondingly more complicated.

Another area of interest is how the BRPH approach, compared with conventional methods, will scale with respect the number of physical dimensions in the scattering problem. It is well-known that the computational effort in DVR calculations, measured by the size of the DVR grid, scales exponentially with the number of degrees of freedom. In BRPH calculations the grid size scales linearly with the number of scattering channels included in the calculation; however, the number of channels also scales exponentially with the number of dimensions. The question will then be, can the BRPH offer a lower pre-exponential factor compared to DVR? The present work indicates that BRPH is advantageous

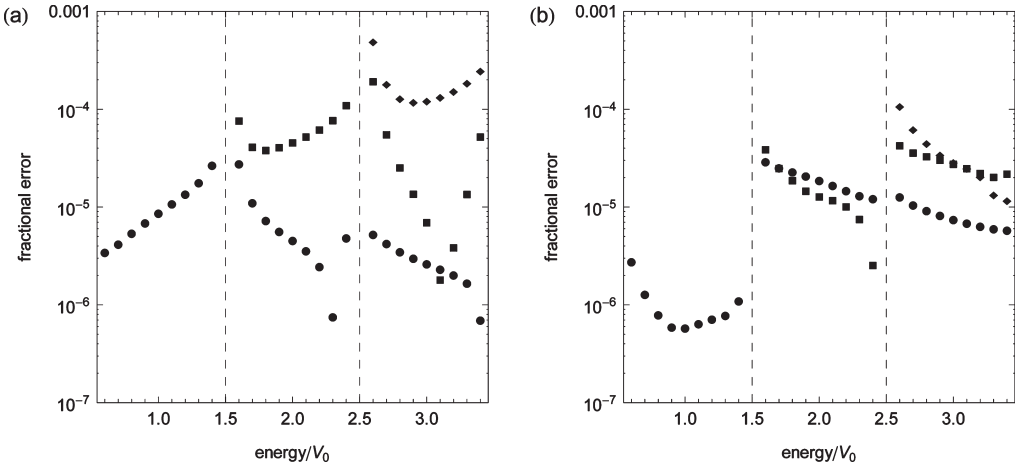

Figure 11. Fractional error estimates for the coupled Eckart+HO problem. Circles, squares, and diamonds represent the $n = 0$, 1, and 2 incident channel states, respectively. Vertical dashed lines indicate the onset of a scattering channel. (a) Fractional error associated with normalization of the partially state-resolved transmission and reflectance probabilities. (b) Fractional error associated with the energy expectation value.

for energies near threshold, and it will be important to establish whether this transfers to curvilinear problems. In any case, however, the primary utility of the BRPH scheme is that it can readily be used in tandem with various approximate methods for describing the bound degrees of freedom. As dimensionality increases, we must ultimately invoke some level of approximation for the solution of the adiabatic eigenvalue problem. These may include harmonic or anharmonic model representations and perturbation theory. For more accurate work, we could also incorporate quantum Monte Carlo representations, supersymmetric quantum mechanics,[58−61] and massively parallel numerical schemes.[62−64] The most appropriate method will likely be dictated by the details of the problem at hand, so it will useful to carefully explore the benefits and limitations associated with a variety of different approaches.

APPENDIX A. DERIVATION OF BRPH EQUATIONS OF MOTION

In this section, we derive the BRPH equations of motion. We begin by constructing the total time derivative of $a_{i\pm}$:

$$\mathrm{d}_t a_{i\pm} = \partial_t a_{i\pm} \pm \frac{p_i}{m} a'_{i\pm} \tag{53}$$

The partial time derivative is simply given by

$$\partial_t a_{i\pm} = -\frac{\mathrm{i}}{\hbar} E a_{i\pm} \tag{54}$$

The convective term contains a spatial derivative of the bipolar components and is evaluated using the expression

$$a'_{i\pm} = \frac{1}{2}(a'_{i+} + a'_{i-}) \pm \frac{1}{2}(a'_{i+} - a'_{i-}) \tag{55}$$

The first term is determined by the FF condition (eq 23). The second term is found by taking the second derivative of the FF condition to give

$$a''_i = \frac{\mathrm{i}}{\hbar} p_i (a'_{i+} - a'_{i-}) \tag{56}$$

and then solving for the difference. Substituting these results back into the total time derivative and rearranging leads to the following equations of motion

$$\mathrm{d}_t a_{i\pm} = \frac{\mathrm{i}}{\hbar}(E - 2E_i) a_{i\pm} - \frac{\mathrm{i}}{\hbar}(E - E_i) a_i + \frac{\mathrm{i}}{\hbar}\left[-\frac{\hbar^2}{2m} a''_i\right] \tag{57}$$

where we note that the last term now contains the second derivative of the scattering amplitude. We appeal to an adiabatic representation of the TISE to evaluate this term. The total stationary state is then expressed as a vector of scattering amplitudes

$$\phi_E = \{a_1, a_2, \ldots\}^T \tag{58}$$

and the TISE can be recast as matrix vector product $\hat{H} \cdot \Phi = E\Phi$, whose elements are given by

$$\sum_j \hat{H}_{ij} a_j = E a_i \tag{59}$$

The matrix elements of the Hamiltonian are functions of x and are formally defined by

$$\hat{H}_{ij} = \int \phi_i^*(x,y) \hat{H} \phi_j(x,y)\, \mathrm{d}y \tag{60}$$

To calculate these more explicitly, we first operate with $\hat{H}$ on the quantity $\phi_j(x,y)\ a(x)$, where the function $a(x)$ serves as a book-keeping factor to help track the order of derivative operators. Applying the Hamiltonian operator and using the adiabatic TISE (eq 19) we obtain

$$\hat{H}(\phi_j a) = -\frac{\hbar^2}{2m}(\phi_j a'' + 2\phi_j^{(1,0)} a' + \phi_j^{(2,0)} a) + \varepsilon_j \phi_j a \tag{61}$$

where we have used the product rule to expand the second derivative in x. Next, we multiply both sides of the equation by $\phi^*_i(x,y)$ and integrate over the y-coordinate to yield

$$\hat{H}_{ij} a = -\frac{\hbar^2}{2m}[\delta_{ij} a'' + I_{ij}^{(1)} a' + I_{ij}^{(0)} a] + \delta_{ij} \varepsilon_i a \tag{62}$$

where we have used the fact that the adiabatic eigenstates are orthonormal. The BRPH integrals $I_{ij}^{(1)}$ and $I_{ij}^{(0)}$ are defined in

eq 29. It is important to note that these quantities are functions of the reaction coordinate that vanish as $x \rightarrow \pm\infty$. Similarly, ε_i are functions of x that converge to a set of fixed eigenvalues that are associated with the vibrational states of the asymptotic reactants or products. Removing the book-keeping factor from the last equation gives form for the matrix elements of the Hamiltonian:

$$\hat{H}_{ij} = -\frac{\hbar^2}{2m}\left[\delta_{ij}\frac{d^2}{dx^2} + I_{ij}^{(1)}\frac{d}{dx} + I_{ij}^{(0)}\right] + \varepsilon_i\delta_{ij} \tag{63}$$

Substituting eq 63 into eq 59 and rearranging the expression for a''_i gives

$$-\frac{\hbar^2}{2m}a_i'' = (E-\varepsilon_i)a_i + \frac{\hbar^2}{2m}\sum_j (I_{ij}^{(1)}a_j' + I_{ij}^{(0)}a_j) \tag{64}$$

Finally, substituting this last expression into eq 57 and rearranging leads to the BRPH equations of motion given in eqs 24 and 28.

APPENDIX B. ANALYTIC FORMULAS FOR BRPH INTEGRALS

In this section we derive analytic expressions for eq 29 in the special case where the potential function $V(x,y)$ along the y-coordinate is described by a displaced and scaled harmonic oscillator. Both the equilibrium position (with respect to the reaction path $y = 0$) and the harmonic frequency (force constant) may vary as a function of x. The potential energy function is given by

$$V(x,y) = V_{\text{scatter}}(x) + \frac{1}{2}m\omega(x)^2(y-Y(x))^2 \tag{65}$$

where V_{scatter} is some 1D barrier potential that depends only on x, m is the reduced mass of the oscillator, $\omega(x)$ is the harmonic frequency, and $Y(x)$ is the equilibrium position. It is assumed that $\omega(x) \rightarrow \omega_0$ and $Y(x) \rightarrow 0$ as $x \rightarrow \pm\infty$, such that the asymptotic potential function is independent of the reaction coordinate. The adiabatic eigenenergies will be given by

$$\varepsilon_i(x) = V_{\text{scatter}}(x) + \hbar\omega(x)\left(i+\frac{1}{2}\right) \tag{66}$$

and asymptotically we have $\varepsilon_i(x \rightarrow \pm\infty) = E_i = \hbar\omega_0(i + 1/2)$.

The adiabatic eigenfunctions for this problem depend parametrically on x and are given by a set of Gauss−Hermite polynomials

$$\phi_j(x,y) = A_j\sqrt{\beta(x)}H_j(u(x,y))\,G(u(x,y)) \tag{67}$$

where $A_j = (2^j j!)^{-1/2}\pi^{-1/4}$ is a normalization factor, $\beta(x) = (m\omega(x)/\hbar)^{1/2}$ is a function with units of inverse length, $H_j(u)$ is the jth Hermite polynomial, and $G(u) = \exp(-u^2/2)$ is a Gaussian function. The Gauss−Hermite polynomials are expressed in terms of the dimensionless function $u(x,y) = \beta(x)(y - Y(x))$.

Expressions for eq 29 are obtained by taking derivatives of eq 67 with respect to x and using well-known results for the moments of the harmonic oscillator eigenfunctions:[65]

$$\int \phi_i{}^* u^0 \phi_n \, dy = \delta_{i,n} \tag{68a}$$

$$\int \phi_i{}^* u^1 \phi_n \, dy = \frac{\sqrt{2}}{2}\left[\sqrt{i+1}\delta_{i,n-1} + \sqrt{i}\delta_{i,n+1}\right] \tag{68b}$$

$$\int \phi_i{}^* u^2 \phi_n \, dy = \frac{1}{2}[\sqrt{(i+2)(i+1)}\delta_{i,n-2} + (2i+1)\delta_{i,n} + \sqrt{i(i-1)}\delta_{i,n+2}] \tag{68c}$$

$$\int \phi_i{}^* u^3 \phi_n \, dy = \frac{\sqrt{2}}{4}[\sqrt{(i+3)(i+2)(i+1)}\delta_{i,n-3} + (3i+3)\sqrt{(i+1)}\delta_{i,n-1} + (3i)\sqrt{i}\delta_{i,n+1} + \sqrt{i(i-1)(i-2)}\delta_{i,n+3}] \tag{68d}$$

$$\int \phi_i{}^* u^4 \phi_n \, dy = \frac{1}{4}[\sqrt{(i+4)(i+3)(i+2)(i+1)}\delta_{i,n-4} + (4i+6)\sqrt{(i+2)(i+1)}\delta_{i,n-2} + (6i^2+6i+3)\delta_{i,n} + (4i-2)\sqrt{i(i-1)}\delta_{i,n+2} + \sqrt{i(i-1)(i-2)(i-3)}\delta_{i,n+4}] \tag{68e}$$

Applying the chain rule to eq 67 and using the properties of Gauss−Hermite polynomials one can show that

$$\phi_j^{(1,0)} = \frac{\beta'}{\beta}\left(-u^2\phi_j + \frac{1}{2}\phi_j + \sqrt{2j}u\phi_{j-1}\right) + \beta Y'(u\phi_j - \sqrt{2j}\phi_{j-1}) \tag{69a}$$

$$\begin{aligned}\phi_j^{(2,0)} = {} & \frac{\beta''}{\beta}\left(-u^2\phi_j + \frac{1}{2}\phi_j + \sqrt{2j}u\phi_{j-1}\right) \\ & + \frac{\beta'^2}{\beta^2}\left(u^4\phi_j - 2u^2\phi_j - \frac{1}{4}\phi_j - \sqrt{8j}u^3\phi_{j-1} + \sqrt{2j}u\phi_{j-1} + \sqrt{4j(j-1)}u^2\phi_{j-2}\right) + \beta^2Y'^2(u^2\phi_j - \phi_j - \sqrt{8j}u\phi_{j-1} \\ & + \sqrt{4j(j-1)}\phi_{j-2}) + \beta Y''(u\phi_j - \sqrt{2j}\phi_{j-1}) \\ & + \beta'Y'(-2u^3\phi_j + 5u\phi_j + \sqrt{32j}u^2\phi_{j-1} - \sqrt{18j}\phi_{j-1} \\ & - \sqrt{16j(j-1)}u\phi_{j-2})\end{aligned} \tag{69b}$$

Substituting eq 69 into eq 29 and using eq 68 we find that

$$I_{ij}^{(1)} = \frac{\beta'}{\beta}(\sqrt{(i+2)(i+1)}\delta_{i,j-2} - \sqrt{i(i-1)}\delta_{i,j+2}) - \sqrt{2}\beta Y'(\sqrt{(i+1)}\delta_{i,j-1} - \sqrt{i}\delta_{i,j+1}) \tag{70a}$$

$$\begin{aligned}I_{ij}^{(0)} = {} & \frac{1}{4}\frac{\beta'^2}{\beta^2}(\sqrt{(i+4)(i+3)(i+2)(i+1)}\delta_{i,j-4} \\ & + \sqrt{i(i-1)(i-2)(i-3)}\delta_{i,j+4}) + \frac{1}{2}\left(\frac{\beta''}{\beta} - \frac{\beta'^2}{\beta^2}\right) \\ & \times(\sqrt{(i+2)(i+1)}\delta_{i,j-2} - \sqrt{i(i-1)}\delta_{i,j+2}) \\ & - \frac{1}{2}\frac{\beta'^2}{\beta^2}(i^2+i+1)\delta_{i,j} + \frac{1}{2}\beta^2Y'^2(\sqrt{(i+2)(i+1)}\delta_{i,j-2} \\ & + \sqrt{i(i-1)}\delta_{i,j+2}) - \frac{\sqrt{2}}{2}\beta Y''(\sqrt{(i+1)}\delta_{i,j-1} - \sqrt{i}\delta_{i,j+1}) \\ & - \frac{1}{2}\beta^2Y'^2(2i+1)\delta_{i,j} - \frac{\sqrt{2}}{2}\beta'Y'(\sqrt{(i+3)(i+2)(i+1)}\delta_{i,j-3} \\ & + \sqrt{i(i-1)(i-2)}\delta_{i,j+3}) + \frac{\sqrt{2}}{2}\beta'Y'(i\sqrt{(i+1)}\delta_{i,j-1} \\ & + (i+1)\sqrt{i}\delta_{i,j+1})\end{aligned} \tag{70b}$$

dx.doi.org/10.1021/ct200566s |J. Chem. Theory Comput. 2011, 7, 3484–3504

There are two interesting subcases. First, if only the harmonic frequency is scaled along the reaction coordinate, then the integrals simplify to

$$I_{ij}^{(1)} = \frac{\beta'}{\beta}(\sqrt{(i+2)(i+1)}\delta_{i,j-2} - \sqrt{i(i-1)}\delta_{i,j+2}) \quad (71a)$$

$$I_{ij}^{(0)} = \frac{1}{4}\frac{\beta'^2}{\beta^2}(\sqrt{(i+4)(i+3)(i+2)(i+1)}\delta_{i,j-4} + \sqrt{i(i-1)(i-2)(i-3)}\delta_{i,j+4}) + \frac{1}{2}\left(\frac{\beta''}{\beta} - \frac{\beta'^2}{\beta^2}\right) \times(\sqrt{(i+2)(i+1)}\delta_{i,j-2} - \sqrt{i(i-1)}\delta_{i,j+2}) - \frac{1}{2}\frac{\beta'^2}{\beta^2}(i^2+i+1)\delta_{i,j} \quad (71b)$$

where we note that there is no coupling between states with different parity. If the oscillator is only displaced along the reaction coordinate, then the integrals reduce to eq 50 of section 4.

APPENDIX C. DVR-ABC CALCULATIONS

In this section, we describe our implementation of the DVR-ABC approach. For the present work, we utilize the universal DVR developed by Miller and Colbert.[54] In 2D problems, this involves a rectangular set of DVR grid points in x and y:

$$q_\alpha = (x_\alpha, y_\alpha) = (\alpha_x\Delta x, \alpha_y\Delta y) \quad (72)$$

where the index $\alpha = 1, 2, ...$, runs over the total number of DVR points and the two subindices $\alpha_x = 0, \pm1, ...$, and $\alpha_y = 0, \pm1, ...$, are used to label the x and y components of the DVR points within the respective x and y subspaces. It is assumed that the problem is more or less centered around the point $(x,y) = (0,0)$ and, for simplicity, that the DVR grid is symmetric along x and along y.

Miller and Seideman[12,13] analyzed flux-correlation functions to develop simple and very useful DVR expressions for computing the cumulative reaction probability and elements of the **S**-matrix; see eqs 76 and 78 below. For a given energy E, these formulas involve the system's Greens function, which in the DVR-ABC approach is constructed via a matrix inversion

$$G = (E\mathbf{I} - H + \mathrm{i}(\Gamma_+ + \Gamma_-)/2)^{-1} \quad (73)$$

where **I** is an identity matrix over the DVR grid points and H is the 2D DVR Hamiltonian:

$$H_{\alpha\beta} = T^{(x)}_{\alpha_x,\beta_x} + T^{(y)}_{\alpha_y,\beta_y} + \delta_{\alpha\beta}V(x_\alpha, y_\alpha) \quad (74)$$

The DVR kinetic energy matrix elements for motion along y are explicitly defined in eq 36, and the expression for x is similar. The quantities $\Gamma_\pm$ in eq 73 define a pair of complex absorbing potentials (CAPs) associated with the asymptotic regions of the scattering system. Like the physical potential, the CAPs are approximated by diagonal matrices over the DVR points. In our work, we use a fourth-order polynomial form

$$(\Gamma_\pm)_{\alpha\beta} = \delta_{\alpha\beta}\begin{cases} Z(x_\alpha \mp X_0)^4/W_x^4 & |x_\alpha| > X_0 \\ 0 & |x_\alpha| \le X_0 \end{cases} \quad (75)$$

where Z, W_x, and X_0 are the CAP height, width, and onset, respectively. Note that the total spatial extent of the DVR grid along x is given by $2(X_0 + W_x)$.

State-to-state reaction probabilities are calculated according to

$$P_{n\to j} = |S_{jn}|^2 = \frac{1}{16\hbar^2}(\phi_j^{\mathrm{DVR}})^*\cdot\Gamma_+\cdot G\cdot\Gamma_-\cdot\phi_n^{\mathrm{DVR}} \quad (76)$$

where ϕ_j^{DVR} (and ϕ_n^{DVR}) is the DVR representation of the asymptotic scattering state associated with channel j (and n). The elements of these vectors are given by

$$(\phi_j^{\mathrm{DVR}})_\alpha = w_\alpha{}^{1/2}(m/p_j)^{1/2}\mathrm{e}^{(\mathrm{i}/\hbar)p_jx_\alpha}\phi_j(y_\alpha) \quad (77)$$

where $w_\alpha = \Delta x\Delta y$ is the 2D DVR weight, $p_j = (2m(E - E_j))^{1/2}$ is the momentum of a particle with kinetic energy $E - E_j$, and $\phi_j(y)$ is a 1D eigenstate of the asymptotic system with eigenenergy E_j. The cumulative reaction probability can be calculated by taking the sum in eq 51 or by using the so-called "direct" expression

$$N(E) = \mathrm{Tr}[\Gamma_-\cdot G\cdot\Gamma_+\cdot G^*] \quad (78)$$

We have used eqs 76 and 78 to the generate the DVR-ABC results for comparison with our BRPH calculations.

DVR-ABC calculations involve a number of parameters that affect the accuracy and convergence of the calculated reaction probabilities. The CAP parameters Z, W_x, and X_0 introduced above are important, and ideally, these should be tuned to completely absorb the outgoing flux over as short a length as possible while minimizing artificial reflections. Similarly, the total spatial extent of the DVR grid along y, which we introduce as the length $2W_y$, must be large enough so that E_j and $\phi_j(y)$ are numerically well-represented. The DVR grid spacings Δx and Δy together with the spatial widths X_0, W_x, and W_y determine the number of DVR grid point and the computational effort of the DVR-ABC calculations. The accuracy of the DVR-ABC calculation may be limited by any one or more of these parameters, and it is generally useful to know the extent to which the calculated reaction probabilities are converged.

To establish the precision of our results, we introduce a length scale defined by the following de Broglie wavelength

$$\lambda = \frac{h}{p} = \frac{2\pi\hbar}{\sqrt{2mE}} \quad (79)$$

Note that we are not implying that λ is associated with any specific physical wave function; rather, we are using it as length scale that can be loosely associated with *both* the bound and scattering components of the true stationary state. Furthermore, we use λ in different ways to set the 2D DVR grid and CAP parameters. For example, we define the grid spacings as

$$\Delta x = \lambda/n_x \quad (80a)$$

$$\Delta y = \lambda/n_y \quad (80b)$$

where n_x and n_y are integers that give the number of points per de Broglie wavelength. The total energy E represents an upper bound for both the kinetic energy of the scattering component and the eigenenergies of the bound states contributing to the true stationary state. Consequently, λ is a lower bound on the physical wavelengths of these components, and the spacings defined by eq 80 are quite useful because the appropriate energy dependence needed to represent the various components is built in. The CAP

parameters are determined by the formulas

$$X_0 = N_0\lambda \tag{81a}$$

$$W_x = N_x\lambda \tag{81b}$$

$$Z = 10E \tag{81c}$$

where N_0 and N_x are integers that determine the width of the spatial grid along x in units of λ.

The spatial extent of the DVR grid along y should cover, at least, the space between the classical turning points defined by the minimum and maximum roots of $V(x) = E$. In fact, the grid should be extended beyond these points to account for the tails of the bound state wave functions associated with tunneling. We have found that λ is not very well-suited for defining W_y; λ is far too large at low energies and becomes much too small as E increases. Instead, we use the following formula

$$W_y = y_{cl} + N_y A^{-1/3} \tag{82a}$$

where N_y is an integer similar to N_x and y_{cl} is the maximum classical turning point along y. Note again, that we are assuming the problem is symmetric about y; if it were not, then one would have an analogous expression for the minimum classical turning point. The parameter A comes from the approximate representation of a 1D wave function in the vicinity of the turning point:

$$\phi(y) \approx \mathrm{Ai}\left(\frac{B + A(y - y_{cl})}{A^{2/3}}\right) \tag{83}$$

where Ai is an Airy function, and the parameters A and B are given by

$$A = 2mV_1/\hbar^2 \tag{84a}$$

$$B = 2m(V_0 - E)/\hbar^2 \tag{84b}$$

Here, V_0 and V_1 are the values of the potential and its first derivative, respectively, evaluated at y_{cl}. The wave function in eq 83 is the well-known solution for a particle evolving under the influence of a linear potential, $V(y) = V_0 + V_1(y - y_{cl})$. The length scale $A^{-1/3}$ is inversely proportional to V_1; therefore, when the force is weak, $A^{-1/3}$ will be large, and the DVR grid will extend further into the forbidden region.

We have established the integers n_x, n_y, N_x, N_y, and N_0 as the tunable parameters for controlling the accuracy of our DVR-ABC calculations, and we have thoroughly investigated the convergence of our DVR-ABC calculations for the Eckart+HO problem. The following protocol has been used to generate converged reaction probabilities. One begins by calculating $N(E)$ using the parameters $n_x = 3$, $n_y = 3$, $N_x = 1$, $N_y = 1$, and $N_0 = 0$. Typically, this gives a very inaccurate result for $N(E)$; nevertheless, this value is saved as a reference. Next, one performs a set of five distinct calculations for $N(E)$, where each integer parameter is increased by 1. The relative difference between the original $N(E)$ and the five updated values is used to estimate the convergence with respect to these parameters. For each parameter a decision is made as to whether to accept the new parameter or continue with the original value. Once the updated parameters are selected, the reference calculation is repeated and the new $N(E)$ is saved. The parameters are sequentially updated again and the convergence is retested. This process is repeated iteratively until the desired precision has been reached or some maximum number of grid points, determined by the computer system's memory, has been exceeded.

In our work, we have set the convergence tolerance to 10^{-5} and the convergence iterations will stop once the reference calculations exceed 4000 DVR points. For the results shown in section 4, the cumulative reaction probabilities converged to a relative difference of 10^{-5} with respect to the integer parameters. The energy points just above the onset of the scattering channels are the exception to this, and these calculations were stopped before this level of convergence could be achieved.

AUTHOR INFORMATION

Corresponding Author

*E-mail: jeremy.maddox@wku.edu.

ACKNOWLEDGMENT

J.B.M. gratefully acknowledges financial support from the Applied Research and Technology Program (ARTP), Western Kentucky University. B.P. gratefully acknowledges support from the Robert A. Welch Foundation (D-1523) and the National Science Foundation (CHE-0741321).

REFERENCES

(1) Maddox, J. B.; Poirier, B. In *Quantum Trajectories*; Hughes, K., Parlant, G., Eds.; Collaborative Computational Project on Molecular Quantum Dynamics (CCP6): Daresbury, UK, 2011; pp 9−11.

(2) Cohen-Tannoudji, C.; Diu, B.; Laloë, F. *Quantum Mechanics*; John Wiley: New York, 1977; pp 32−34.

(3) Tannor, D. J. *Introduction to Quantum Mechanics: A Time-Dependent Perspective*; University Science Books: Sausalito, CA, 2007; pp xv−xvi.

(4) Steinfeld, J. I.; Francisco, J. S.; Hase, W. L. *Chemical Kinetics and Dynamics*; Prentice-Hall: Englewood Cliffs, NJ, 1989; pp 268−272.

(5) Levine, R. D.; Bernstein, R. B. *Molecular Reaction Dynamics and Chemical Reactivity*; Oxford University Press: New York, 1987; pp 276−289.

(6) Lill, J. V.; Parker, G. A.; Light, J. C. *Chem. Phys. Lett.* **1982**, *89*, 483–489.

(7) Lill, J. V.; Parker, G. A.; Light, J. C. *J. Chem. Phys.* **1986**, *85*, 900–910.

(8) Light, J. C.; Hamilton, I. P.; Lill, J. V. *J. Chem. Phys.* **1985**, *82*, 1400–1409.

(9) Whitnell, R. M.; Light, J. C. *J. Chem. Phys.* **1987**, *86*, 2007–2019.

(10) Engquist, B.; Majda, A. *Proc. Natl. Acad. Sci. U. S. A.* **1977**, *74*, 1765–1766.

(11) Neuhasuer, D.; Baer, M. *J. Chem. Phys.* **1989**, *90*, 4351–4355.

(12) Seideman, T.; Miller, W. H. *J. Chem. Phys.* **1992**, *96*, 4412–4422.

(13) Seideman, T.; Miller, W. H. *J. Chem. Phys.* **1992**, *97*, 2499–2514.

(14) Thompson, W. H.; Miller, W. H. *Chem. Phys. Lett.* **1993**, *206*, 123–129.

(15) Auerbach, S. M.; Miller, W. H. *J. Chem. Phys.* **1994**, *100*, 1103–1112.

(16) Wang, H.; Thompson, W. H.; Miller, W. H. *J. Chem. Phys.* **1997**, *107*, 7194–7201.

(17) Poirier, B.; Miller, W. H. *Chem. Phys. Lett.* **1997**, *265*, 77–83.

(18) Edlund, A.; Peskin, U. *Int. J. Quantum Chem.* **1998**, *69*, 167–173.

(19) Gezelter, J. D.; Miller, W. H. *J. Chem. Phys.* **1995**, *103*, 7868–7876.

(20) Seideman, T. *J. Chem. Phys.* **1993**, *98*, 1989–1998.

(21) Thompson, W. H.; Miller, W. H. *J. Chem. Phys.* **1994**, *101*, 8620–8627.
(22) Peskin, U.; Miller, W. H. *J. Chem. Phys.* **1995**, *102*, 4084–4092.
(23) Thompson, W. H.; Karlsson, H. O.; Miller, W. H. *J. Chem. Phys.* **1996**, *105*, 5387–5396.
(24) Gezelter, J. D.; Miller, W. H. *J. Chem. Phys.* **1996**, *104*, 3546–3554.
(25) Qi, J.; Bowman, J. M. *J. Chem. Phys.* **1996**, *104*, 7545–7553.
(26) Saalfrank, P.; Miller, W. H. *Surf. Sci.* **1994**, *303*, 206–230.
(27) Poirier, B.; Carrington, J.; Tucker *J. Chem. Phys.* **2003**, *118*, 17–28.
(28) Poirier, B.; Carrington, J.; Tucker *J. Chem. Phys.* **2003**, *119*, 77–89.
(29) Muga, J. G.; Palao, J. P.; Navarro, B.; Egusquiza, I. L. *Phys. Rep.* **2004**, *395*, 357–426.
(30) Poirier, B. *J. Chem. Phys.* **2004**, *121*, 4501–4515.
(31) Trahan, C.; Poirier, B. *J. Chem. Phys.* **2006**, *124*, 034115/1–034115/18.
(32) Trahan, C.; Poirier, B. *J. Chem. Phys.* **2006**, *124*, 034116/1–034116/14.
(33) Poirier, B. *J. Theor. Comput. Chem.* **2007**, *6*, 99–125.
(34) Poirier, B.; Parlant, G. *J. Phys. Chem. A* **2007**, *111*, 10400–10408.
(35) Poirier, B. *J. Chem. Phys.* **2008**, *129*, 084103/1–084103/18.
(36) Poirier, B. *J. Chem. Phys.* **2008**, *128*, 164115/1–164115/15.
(37) Park, K.; Poirier, B.; Parlant, G. *J. Chem. Phys.* **2008**, *129*, 194112/1–194112/16.
(38) Park, K.; Poirier, B. *J. Theor. Comput. Chem.* **2010**, *9*, 711–734.
(39) Wyatt, R. E. *Quantum Dynamics with Trajectories: Introduction to Quantum Hydrodynamics*; Springer: New York, 2005; pp 11−21.
(40) Miller, W. H.; Handy, N. C.; Adams, J. E. *J. Chem. Phys.* **1980**, *72*, 99–112.
(41) Fast, P. L.; Truhlar, D. G. *J. Chem. Phys.* **1998**, *109*, 3721–3729.
(42) Gonzalez, J.; Gimenez, X.; Bofill, J. M. *Theor. Chem. Acc.* **2004**, *112*, 75–83.
(43) Fernandez-Ramos, A.; Ellingson, B. A.; Garrett, B. C.; Truhlar, D. G. *Rev. Comp. Chem.* **2007**, *23*, 125–232.
(44) Gonzalez, J.; Gimenez, X.; Bofill, J. M. *J. Chem. Phys.* **2009**, *131*, 054108/1–054108/16.
(45) Fang, J.-Y.; Hammes-Schiffer, S. *J. Chem. Phys.* **1998**, *108*, 7085–7099.
(46) Fang, J.-Y.; Hammes-Schiffer, S. *J. Chem. Phys.* **1998**, *109*, 7051–7063.
(47) Hinkle, C. E.; McCoy, A. B. *J. Phys. Chem. Lett.* **2010**, *1*, 562–567.
(48) Presently, all CPWMs require the scattering potential to converge asymptotically. For example, asymptotically periodic potentials are beyond the scope of existing CPWMs; however, we see no reason why the CPWM approach could not be extended to such problems, for example, by using Bloch-type bipolar components.
(49) The form of the effective potential does make a difference in numerical applications and should ideally be a smooth, slowly varying function connecting the asymptotic values of $V(x)$.
(50) Fröman, N.; Fröman, P. O. *JWKB Approximation*; North-Holland: New York, 1965.
(51) Ahmed, Z. *Phys. Rev. A* **1993**, *47*, 4761–4767.
(52) Abramowitz, M.; Stegun, I. A. *Handbook of Mathematical Functions with Formulas, Graphs, and Mathematical Tables*; Dover Publications: New York, 1965; pp 877−898.
(53) Please note the distinction between the index i and the imaginary unit $\mathrm{i} = (-1)^{1/2}$.
(54) Colbert, D. T.; Miller, W. H. *J. Chem. Phys.* **1992**, *96*, 1982–1991.
(55) Press, W. H.; Teukolsky, S. A.; Vetterling, W. T.; Flannery, B. P. *Numerical Recipes in Fortran: The Art of Scientific Computing*, 3rd ed.; Cambridge University Press: New York, 2007; pp 155−162; 907−910
(56) Datta, S. *Quantum Transport: Atom to Transitor*; Cambridge University Press: New York, 2005; pp 17−18.
(57) Pauler, D. K.; Kendrick, B. K. *J. Chem. Phys.* **2004**, *120*, 603–611.
(58) Bittner, E. R.; Maddox, J. B.; Kouri, D. J. *J. Phys. Chem. A* **2009**, *113*, 15276–15280.
(59) Kouri, D. J.; Markovich, T.; Maxwell, N.; Bittner, E. R. *J. Phys. Chem. A* **2009**, *113*, 15257–15264.
(60) Kouri, D. J.; Maji, K.; Markovich, T.; Bittner, E. R. *J. Phys. Chem. A* **2010**, *114*, 8202–8216.
(61) Kouri, D. J.; Maji, K.; Markovich, T.; Bittner, E. R. *J. Phys. Chem. A* **2011**, *115*, 950.
(62) Chen, W.; Poirier, B. *J. Theor. Comput. Chem.* **2010**, *9*, 825–846.
(63) Chen, W.; Poirier, B. *J. Theor. Comput. Chem.* **2010**, *9*, 435–469.
(64) Yang, B.; Chen, W.; Poirier, B. *J. Chem. Phys.* **2011**, *135*, 094306/1–094306/17.
(65) Wilson, E. B.; Decius, J. C.; Cross, P. C. *Molecular Vibrations: The Theory of Infrared and Raman Vibrational Spectra*; McGraw-Hill Book Company, Inc.: New York, 1955; pp 289−291.